Chemical Engineering Science 146 (2016) 259–290

Contents lists available at ScienceDirect

Chemical Engineering Science

journal homepage: www.elsevier.com/locate/ces

Comprehensive experimental investigation of counter-current bubble column hydrodynamics: Holdup, flow regime transition, bubble size distributions and local flow properties

Giorgio Besagni*, Fabio Inzoli

Politecnico di Milano, Department of Energy, Via Lambruschini 4a, 20156 Milano, Italy

HIGHLIGHTS

- We experimentally study a large-diameter counter-current bubble column.
- We compare the results obtained with different experimental methods.
- We investigate the flow regime transition.
- We analyse bubble size distributions and shapes in the developed region and near the sparger.
- We provide optical probe measurements at different axial and radial positions.

ARTICLE INFO

Article history:
Received 30 September 2015
Received in revised form
28 January 2016
Accepted 28 February 2016
Available online 4 March 2016

Keywords:
Bubble column
Holdup
Counter-current
Optical probe
Bubble size distribution
Flow regime transition

ABSTRACT

In this paper, we apply a variety of experimental techniques to investigate the influence of the counter-current mode on bubble column hydrodynamics. We study an air–water bubble column, which is 5.3 m in height and has an inner diameter of 0.24 m, and we consider gas superficial velocities in the range of 0.004–0.20 m/s and liquid superficial velocities up to −0.09 m/s. The experimental investigation consists of holdup, gas disengagement, image analysis and optical probe measurements. The holdup measurements are compared with the literature and are used to investigate the flow regime transition. The gas disengagement measurements are used to further investigate the flow regime transition and study the structure of the holdup curve. The image analysis is used to study the bubble shapes and size distributions near the sparger and in the developed region of the column; in particular, the image analysis is applied to different gas velocities in the homogeneous regime in both the batch and counter-current modes. The optical probe is used to acquire radial profiles of the local properties (i.e., local void fraction and bubble rise velocity) to study the flow properties and further investigate the flow regime transition. Comparing the results from the different techniques, the influence of the gas superficial velocity and the liquid superficial velocity is discussed considering all main aspects of the two-phase flow, from the local flow properties to the global flow features. The counter-current mode is found to increase the holdup, reduce the bubble rise velocity, destabilize the homogeneous regime and change the local flow properties.

1. Introduction

Bubble columns are frequently used in chemical and biochemical engineering. Their main advantage is a large contact area between the liquid and gas phases and good mixing within the liquid phase. The correct design and operation of these devices rely on the proper prediction of the flow pattern and global and local flow properties—i.e., the holdup (ε_G), bubble rise velocity (u_b), local void fraction ($\varepsilon_{G,Local}$) and bubble size distributions (BSDs). The global and local flow properties are related to the prevailing flow regime: mainly, the homogeneous and heterogeneous regimes. The former is associated with small superficial gas velocities (U_G) and is characterized by the presence of small, uniformly sized bubbles with little interaction. The latter is associated with high gas superficial velocities, high coalescence and breakage phenomena and a wide variety of bubble sizes. Eventually, when a sparger with large openings is used, the quality of the gas distribution is poor,

* Corresponding author. Tel.: +39 02 2399 8431.
E-mail addresses: giorgio.besagni@polimi.it (G. Besagni), fabio.inzoli@polimi.it (F. Inzoli).

http://dx.doi.org/10.1016/j.ces.2016.02.043
0009-2509/

and a gas maldistribution regime is established at low U_G values (Nedeltchev and Schubert, 2015). The transition from the homogeneous regime to the heterogeneous regime is a gradual process in which a transition flow regime occurs. This regime is characterized by large flow macro-structures with large eddies and widened bubble size distribution owing to the onset of bubble coalescence. The global and local flow properties (and the flow regimes) are also related to the bubble column operation mode: the batch ($U_L \approx 0$ m/s), the co-current ($U_L > 0$ m/s) or the counter-current ($U_L < 0$ m/s) mode (Deckwer, 1992; Leonard et al., 2015; Rollbusch et al., 2015b). Whereas the co-current or semi-batch modes are widely studied, the counter-current mode is significantly less frequently investigated (Leonard et al., 2015).

In this paper, we apply a variety of experimental techniques to investigate the influence of the counter-current mode on holdup, regime transition, local flow properties and bubble size distributions. We study an air–water bubble column ($H_c = 5.3$ m height and $d_c = 0.24$ m inner diameter, aspect ratio $H_c/d_c > 20$) and consider gas superficial velocities in the range of 0.004–0.20 m/s and liquid superficial velocities up to -0.09 m/s. The diameter of the column and its height were chosen considering the well-known scale-up criteria for the results: $d_c > 0.15$ m and $H_c/d_c > 5$ (Kantarci et al., 2005; Leonard et al., 2015). The column diameter classifies this facility as a large-diameter pipe, considering the dimensionless diameter D_H^* proposed by Kataoka and Ishii (1987):

$$D_H^* = \frac{D_H}{\sqrt{\sigma / g(\rho_L - \rho_G)}} \tag{1}$$

where D_H is the hydraulic diameter, σ is the surface tension coefficient, g is the gravity acceleration, and $\rho_L - \rho_G$ is the density difference between the two phases. Columns with dimensionless diameters greater than the critical value $D_{H,Cr}^* = 52$ are considered to be large-diameter columns (Brooks et al., 2012), and the present bubble column has a dimensionless diameter $D_H^* = 88.13$. When the column diameter is larger than the critical value, the stabilizing effect of the channel wall on the interface of the Taylor bubbles decreases, and the slug flow can no longer be sustained because of the Rayleigh–Taylor instabilities. The hydrodynamic properties in large-diameter columns differ from the flow in small-diameter columns and the flow regime maps and flow regime transition criteria used to predict the behavior of two-phase flow in small-diameter columns may not be scaled up to understand and predict the flow in large ones (Shawkat and Ching, 2011). Therefore, ad-hoc experimental studies are needed for establishing a reliable dataset, especially for counter-current large-diameter bubble columns, owing to the lack of research. In the remainder of the introduction, we propose a literature survey about the influence of the liquid velocity over holdup, flow regime transition, local flow properties and bubble size distributions.

Low liquid velocities do not affect the holdup—as found by several investigators (Akita and Yoshida, 1973; de Bruijn et al., 1988; Lau et al., 2004; Rollbusch et al., 2015a; Sangnimnuan et al., 1984; Shah et al., 1982; Shawaqfeh, 2003; Voigt and Schügerl, 1979; Yang and Fan, 2003)—because, if U_L is low compared with the bubble rise velocities, the acceleration of the bubbles is negligible (Hills, 1976). For example, Akita and Yoshida (1973) ($d_c = 0.152$ m, $H_c = 2.5$ m) observed a negligible effect of U_L (up to 0.04 m/s) in both co-current and counter-current operations. At higher liquid velocities, the column operation influences the holdup: the co-current mode reduces the holdup (Biń et al., 2001; Chaumat et al., 2005b; Jin et al., 2007; Kumar et al., 2012; Otake et al., 1981; Pjontek et al., 2014; Shah et al., 2012; Simonnet et al., 2007), and the counter-current mode increases the holdup (Besagni and Inzoli, 2016a; Besagni et al., 2014, 2015; Biń et al., 2001; Jin et al., 2010; Otake et al., 1981) as bubbles are either accelerated or decelerated by liquid motion (Leonard et al., 2015; Rollbusch et al., 2015a). Baawain et al. (2007) showed that the counter-current or co-current operation modes influenced the holdup by approximately 5% in weight, and less than 1% in bubble size, showing that the effect observed is mainly caused by the bubble rise velocity and not only the bubble size. Biń et al. (2001) showed that the holdup increases with increasing U_L in counter-current mode and decreases (or remains constant) in co-current mode. The effect is more pronounced at high gas velocities, and the difference in the holdup between co-current and counter-current mode is approximately 10%. The same trends were observed by Jin et al. (2010) ($d_c = 0.160$ m, $H_c = 2.5$ m), who reported a maximum difference of 2% between counter-counter and co-current modes. Similar trends were found by Otake et al. (1981) ($d_c = 0.05$ m, $H_c = 1.5$ m). Besagni et al. (2014, 2015) ($d_c = 0.24$ m, $H_c = 5.3$ m), (Besagni and Inzoli, 2016a) found that the counter-current mode influences the column hydrodynamics affecting both the holdup and the local flow properties in annular gap and open tube (with a "*pipe-sparger*") bubble columns. Their analysis covered gas superficial velocities up to 0.26 m/s and liquid superficial velocities up to -0.11 m/s. It appears that the influence of the operation mode is lower at high holdup (Besagni and Inzoli, 2016a; Besagni et al., 2014, 2015; Jin et al., 2010). With regard to the regime transition, Jin et al. (2010) reported that the transition point is the same among the three working modes if U_L is lower than 0.04 m/s, whereas for higher U_L (in co-current and counter-current modes), the transition velocity decreases with increasing superficial liquid velocity. Otake et al. (1981) observed an earlier regime transition increasing the liquid flowrate in the counter-current mode (U_L up to -0.15 m/s). Similar conclusions were drawn by Yamaguchi and Yamazaki (1982a) ($d_c = 0.04$ m and 0.08 m), Besagni et al. (2014, 2015) and Besagni and Inzoli (2016a). It is worth noting that the hydrodynamic properties of bubble columns are determined by the momentum exchange between the liquid and gas phases. Therefore, the flow in a bubble column is governed by the same mechanisms as in other pipe flows. In this respect, Besagni et al. (2015) proposed a survey on counter-current flow in vertical pipes; as a result, most of the studies focused on small-diameter pipes, and our experimental setup ($D_H^* = 88.13$) covers a range in which there is a lack of studies.

The holdup is also a function of the axial and radial position in the column. The spatial variation of the holdup gives rise to pressure variation, which results in liquid recirculation in the bubble column (which governs the rate of mixing, heat transfer and mass transfer). Knowledge of the local void fraction profiles would help in determining the flow regimes, liquid mixing, and heat and mass transfer, and knowledge of the local flow properties would help in the Computational Fluid Dynamics (CFD) model validation. Local void fraction holdup profiles may be center peaked, wall peaked or flat, depending on U_G, U_L, the column design, the sparger design, the nature of the gas–liquid system and the operating conditions. During recent decades, many experimental measurements of holdup profiles have been reported by using a variety of techniques, as reviewed by Joshi et al. (1998). Among the different techniques, we employed needle probes. In general, two types of needle probes have been previously used for measurement in bubble columns: optical fiber and impedance/conductive probes (Boyer et al., 2002). Optical and impedance probes operate based on the differences in the refractive index or conductivity, respectively, of the liquid and gas phases. In this study, dual-tipped optical probes have been used: these devices are capable of simultaneously measuring local holdups, bubble chord lengths and rise velocities (Chabot et al., 1998; Chaumat et al., 2007; Magaud et al., 2001; Moujaes, 1990; Shiea et al., 2013).

In addition to the holdup, another important parameter of bubble column hydrodynamics is the Bubble Size Distribution (BSD). The BSD generated at the sparger gradually changes along the column owing to coalescence and break-up phenomena until reaching an equilibrium/developed BSD. Along with the holdup, the BSD provides an evaluation of the interfacial area (Kantarci

et al., 2005) and is an important parameter for the setup and validation of CFD models (Lucas et al., 2015). In fact, when setting up an Euler multi-fluid model, a bubble diameter or a BSD is requested as an input, and if considering the bubble-coalescence and -breakup models, the BSD at both the sparger and in the developed region should be considered (the former for input and the latter for validation). In the literature, different intrusive and nonintrusive techniques have been proposed for measuring the bubble size distribution and bubble shape (Busciglio et al., 2010; Rodrigues and Rubio, 2003; Xu and Shepard, 2014). Nonintrusive measurement techniques are preferred over intrusive methods because the flow conditions are not disturbed, and image analysis is attracting growing attention. Image analysis has been mostly applied to rectangular/small-scale (Lau et al., 2013a, 2013b; Zaruba et al., 2005) or medium scale (Schäfer et al., 2002) bubble columns, but there is a lack of studies concerning BSDs in large-diameter bubble columns. Furthermore, studies analyzing the bubble size distributions near the sparger are uncommon (Hur et al., 2013), and the influence of the liquid velocity on the bubble shape and bubble size distribution is far from being understood (Besagni and Inzoli, 2016b). In the present study, we have applied a method based on human recognition of the bubble edge (Besagni et al., 2015; Besagni and Inzoli, 2016b). This method was selected because, despite different image-processing algorithms that have been proposed, these techniques are still limited to resolve large bubble clusters, highly unsteady flows, and large void fractions (Karn et al., 2015). Additionally, at low holdup, there are problems associated with overlapping: if the holdup exceeds 1%, more than 40% of the bubbles are overlapping in the image (Lecuona et al., 2000; Rodríguez-Rodríguez et al., 2003). Various studies have addressed this problem and have proposed different methods for dealing with overlapping bubbles (Lau et al., 2013b); however, no agreement has been reached, and some approaches may cause a significant reduction of the bubble sample size and an underestimation of the bubble diameter.

In this paper, we experimentally investigate the influence of the counter-current mode on bubble column hydrodynamics. Holdup, local holdups, local bubble velocities, bubble size distribution and shape parameters are measured by a wide variety of techniques, and results obtained with different methods are compared. Specifically, in this study, we use (i) holdup measurements, (ii) gas disengagement technique, (iii) image analysis and (iv) optical probe. The holdup measurements are compared with the literature and are used for investigating the regime transition. The gas disengagement technique is then used for further investigating the regime transition and describing the holdup structure. An image analysis technique is applied to quantify the bubble size distribution and bubble shape near the sparger and in the developed region. The image analysis is applied for five superficial gas velocities in the homogeneous regime—up the transition point—in both the batch and counter-current modes. Finally, the optical probe is used to acquire the radial profiles of the local flow properties (local void fraction, bubble rise velocity and bubble size) at two axial positions to study the flow structures and further investigate the regime transition. The paper is structured as follows. In Section 2, the experimental setup and the measurement techniques are detailed. In Section 3, the experimental results are presented, and in Section 4 the conclusions are given.

2. Experimental setup and method

2.1. Experimental setup

The experimental facility (Fig. 1) is a non-pressurized vertical pipe made of Plexiglas with height $H_c = 5.3$ m and inner diameter $d_c = 0.24$ m. A pressure reducer controls the pressure upstream of the rotameters (1) and (2), used to measure the gas flowrate (accuracy $\pm 2\%$ f.s.v., E5-2600/h, manufactured by ASA, Italy). A pump, controlled by a bypass valve, provides water recirculation, and a rotameter (3) measures the liquid flowrate (accuracy $\pm 1.5\%$ f.s.v., G6-3100/39, manufactured by ASA, Italy). The air distributor, is a "*spider-sparger*" with hole diameters $d_o = 2$–4 mm (Fig. 2a). Filtered air and clean filtered deionized water were used; during the experiments, the air and water temperatures were maintained constant at room temperature (22 ± 1 °C).

The values of gas density (used to compute the superficial gas velocity, U_G) are based upon the operating conditions existing at the column midpoint. The midpoint column pressure is assumed to be equal to the column outlet pressure plus one-half the total experimental hydrostatic pressure head (Reilly et al., 1994).

2.2. Holdup measurements

2.2.1. Measurements

Measurements of the bed expansion allowed the evaluation of the holdup ε_G. The procedure involves measuring the location (height) of liquid free surface when air flows in the column. The holdup is then obtained using the relation:

$$\varepsilon_G = \frac{(H_D - H_0)}{H_D} \tag{2}$$

where H_D and H_0 are the heights of the free-surface after and before aeration, respectively ($H_0 = 3.4$ m from the bottom of the column and $H_0 = 3.0$ m from the sparger).

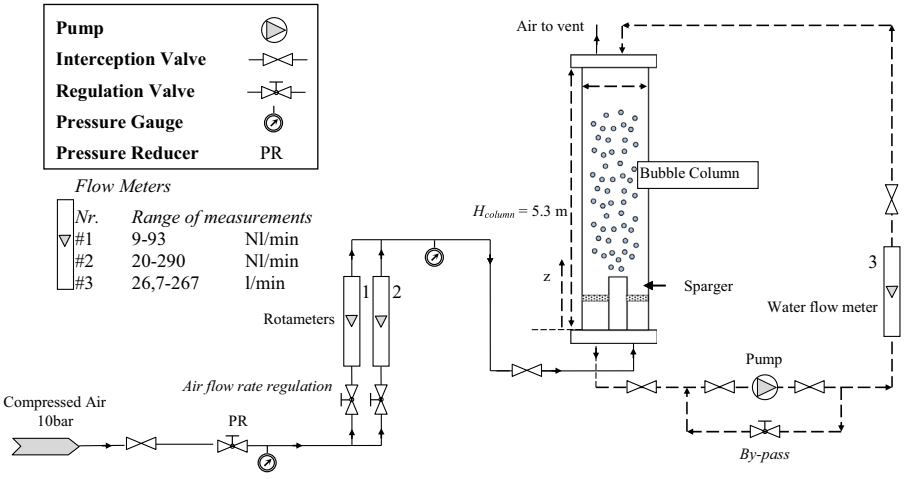

Fig. 1. Experimental setup.

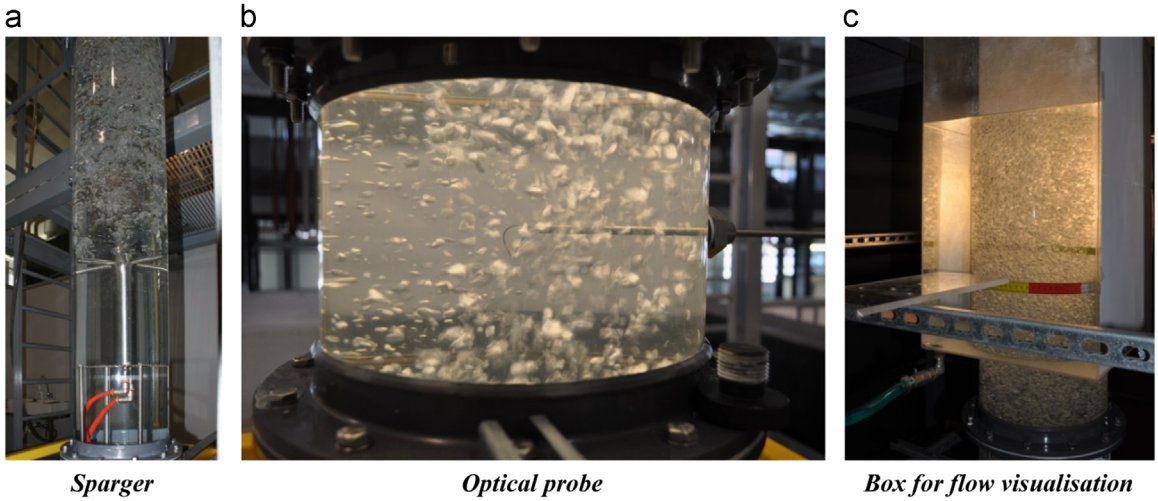

Fig. 2. Experimental setup and measurement techniques.

2.2.2. Flow regime transition

Two main transitions exist in large-diameter bubble columns: (i) the transition between the homogeneous and transition regimes and (ii) the transition between the transition and the heterogeneous regimes. However, in the literature, many authors consider only the first regime transition, without any reference to the second one, except for a limited number of studies (Nedeltchev, 2015; Nedeltchev and Shaikh, 2013). In the following, for the sake of clarify, we refer to "*flow regime transition point*" considering the first transition. Although the transition from the homogeneous to the heterogeneous regime does not occur instantaneously, the definition of an approximate transition point is helpful to model the hydrodynamic behavior of bubble columns (Krishna et al., 1991).

We use two statistical methods to study the flow regime transition.

2.2.2.1. Swarm velocity method. The *swarm velocity method* was developed by Zuber and Findlay (1965) and is based on the swarm velocity:

$$U_{swarm} = U_G/\varepsilon_G \tag{3}$$

The swarm velocity is plotted against the superficial gas velocity: U_{swarm} is almost constant in the homogeneous regime (in some cases, it can be slightly decreasing), but it starts to increase as the system enters the heterogeneous regime at a transition superficial velocity U_{trans}. The appearance of the first large bubble is responsible for this sudden increase in swarm velocity and is an indication of flow regime transition. This method has previously been employed by Krishna et al. (1991), Letzel et al., (1997), Gourich et al., (2006), Ribeiro and Mewes (2007), Besagni et al. (2014, 2015) and Besagni and Inzoli (2015, 2016a, 2016b). In this study, the quantitative evaluation of U_{trans} is determined by the intersection between the trends of U_{swarm} in the two regimes. U_{swarm} is constant for the homogeneous regime.

U_{swarm} is constant for the homogeneous regime:

$$U_{swarm,homogeneous} = cons \tag{4}$$

whereas, in the heterogeneous/transition regime is determined by a least squares fitting of the following function:

$$U_{swarm,heterogeneous} = S_1(U_G)^{S_2} + S_3 \tag{5}$$

where S_1, S_2 and S_3 are fitting parameters. The transitional velocity is then evaluated by solving the following equation:

$$U_{swarm,homogeneous} = U_{swarm,heterogeneous} \tag{6}$$

2.2.2.2. Drift-flux method. The *drift-flux method* was proposed by Wallis (Wallis, 1969) and has been widely applied in the literature (Besagni et al., 2015; Besagni and Inzoli, 2015, 2016a, 2016b; Passos et al., 2015; Ribeiro Jr and Mewes, 2007; Wallis, 1969). This method is based on the drift flux, which represents the gas flux through a surface moving with the speed of the two-phase mixture and is experimentally obtained as follows:

$$J_T = U_G(1-\varepsilon_G) \pm U_L\varepsilon_G \tag{7}$$

which, for a counter-current flow, reads as follows:

$$J_T = U_G(1-\varepsilon_G) + U_L\varepsilon_G \tag{8}$$

Please refer to the discussion proposed by Besagni and Inzoli (Besagni and Inzoli, 2016a) for the detailed derivation of Eq. (7) and (8).

Theoretically, the drift flux is written in terms of the bubble swarm velocity, whose dependence upon ε_G varies with the prevailing regime:

$$J_E = U_b(1-\varepsilon_G) \tag{9}$$

The idea in this method is to employ a model for U_b that is valid for the homogeneous regime, plotting J_E and J_T in the same graph as a function of ε_G. In the homogeneous regime, J_E is equal to J_T and the transition point is defined when:

$$J_T \neq J_E \tag{10}$$

The evaluation of U_b is a matter of discussion in the literature, and different models have been proposed and applied. In this study, we follow the approach of Krishna et al. (2000), which is based on the empirical model of Richardson and Zaki (1997):

$$U_b = u_\infty(1-\varepsilon_G)^{n-1} \tag{11}$$

where n is fluid-dependent ($n \cong 2$ for water) and should be fitted with the aid of the experimental data, together with u_∞, the terminal velocity of an isolated bubble, in the determination of the regime transition point. Combining Eqs. (9) and (11), we obtain the following:

$$J_E = u_\infty\varepsilon_G(1-\varepsilon_G)^n \tag{12}$$

2.3. Gas disengagement technique

The structure of the gas phase and the flow regime transition are further investigated by the gas disengagement (GD) technique

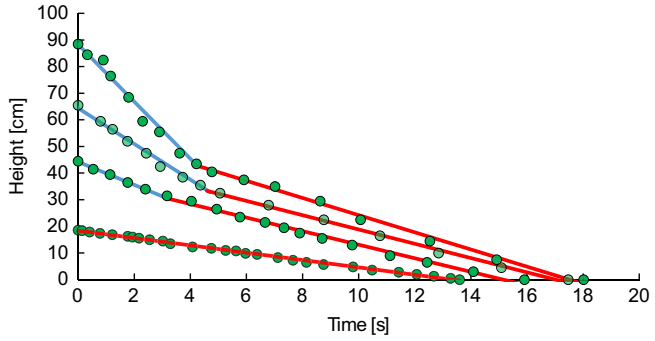

Fig. 3. The gas disengagement technique: curves obtained in the homogeneous and transition regimes.

using a camera. By recording the drop in dispersion height after stopping the gas supply and following the procedure of Schumpe and Grund (1986), we may evaluate the contributions of the "*coalescence-induced*" (CI) and the "*non-coalescence-induced*" (NCI) bubbles. The GD technique has been widely discussed and applied in the literature. Fig. 3 presents an example of the GD profiles obtained in this study (homogeneous and heterogeneous regimes). Despite this technique having been widely applied in the literature, its assumptions should be noted:

- the dispersion is axially homogeneous when the gas flow is interrupted;
- there are no interactions between "*coalescence-induced*" and the "*non-coalescence-induced*" bubbles (coalescence and break-up are neglected);
- the rate of the disengagement process is constant ("*coalescence-induced*" bubbles do not influence "*non-coalescence-induced*" and vice-versa).

The problems related to the deviations from these assumptions (i.e., in coalescing systems at high U_G) have been discussed elsewhere and will not be repeated here (Deshpande et al., 1995; Schumpe and Grund, 1986).

2.4. Optical probe

The local flow properties were measured using a double fiber optical probe. The optical probe is inserted, via an access port (Fig. 2c), into the flow at a height of $h_{probe}=2.3$ m from the bottom of the column ($h_{probe}=1.9$ m from the sparger) and at $h_{probe}=1.1$ m ($h_{probe}=0.7$ m from the sparger).

2.4.1. Instrumentation

A double-fiber optical probe system (manufactured by RBI) measures local flow properties (local void fraction, bubble vertical velocity, bubble Sauter mean diameter, interfacial area and bubble chord length distributions). Similar optical probe system have been used by different authors (Besagni et al., 2014, 2015; Besagni and Inzoli, 2015, 2016a; Chaumat et al., 2005a; Kiambi et al., 2003; Lima Neto et al., 2008; Simonnet et al., 2007; Zhang and Zhu, 2013).

Optical probes distinguish the gas and liquid phases by measuring the intensity of a laser light that is reflected and/or refracted at the probe tip on the basis of the refractive indexes of the probe tip, gas and liquid phases (Barrau et al., 1999). The probe signal is measured via an optoelectronic module, which emits the laser to the probe tip and converts the reflected optical signal into a digital signal. From the digital signal, the bubble frequency f (bubble number per unit time) and void fraction $\varepsilon_{G,Local}$ (assuming it equals the proportion of time when the tip is surrounded by gas) can be obtained. By cross-correlating the signals from the two tips, the bubble traveling time from one tip to the other can be estimated, and the bubble velocity u_b can be calculated. Assuming that bubbles are spherical, bubble Sauter mean diameter d_b, is calculated by the optical probe system:

$$d_b = 3\varepsilon_{G,Local}u_b/2f \tag{13}$$

Eq. (13) is based on the assumption of spherical bubbles; however, this assumption is only approximately valid when bubbles are small. The following equation has been used to account for the non-sphericity of bubbles (Simonnet et al., 2007):

$$d_{b,corrected} = \varphi^{-2/3}3\varepsilon_{G,Local}u_b/2f \tag{14}$$

where φ is the aspect ratio.

In this study, all the measurements have been obtained using a sampling period equal to $\Delta t_{sampling}=1000$ s, which is large enough to produce reliable time-averaged values. Moreover, this measurement period is far above the typical values of 1–5 min for similar optical probes (Chang et al., 2003; Chaumat et al., 2005a; Lima Neto et al., 2008; Zhang and Zhu, 2013).

2.4.2. Optical probe sources of errors

When considering the experimental error of the optical probes, two aspects should be considered. The first is the statistical error associated with the measuring time, which is proportional to the square root of the measuring time: in our case, the absolute uncertainty in the gas fraction is approximately 0.001. The second aspect is a bias error due to the difficulties of piercing a bubble at the bubble edge (Vejražka et al., 2010):

- improper dewetting at the probe tip (the *blinding effect*);
- alteration of bubble trajectory prior to or during the piercing process (the *drifting effect*);
- bubble deformation and/or deceleration at the probe tip (the *crawling effect*).

Both the blinding effect and the crawling effect include deformation effects. The deformation of the blinding effect is mainly related to a local deformation zone located in the bubble interface, which may be produced by both the probe-induced liquid pressure over the bubble and the direct impact itself. The crawling effect considers the deformation of large parts of the bubble. The relative influence of these effects on the final residence time estimates, as well as their absolute magnitude, is not yet clear. A summary of the errors reported by the optical probe in the literature is as follows:

- *Void fraction.* Generally, the optical probe is considered rather accurate in terms of void fraction. Comparing optical probe results with other measurement techniques (i.e., visual or pressure sensors), the relative differences found in the literature are as follows: between −0.8% and −16% (Barrau et al., 1999), −2.2% (Zhang and Zhu, 2013), - 3% (Chang et al., 2003), −11% (Lima Neto et al., 2008), between −6 and −14% (Kiambi et al., 2003), +12% (Simonnet et al., 2007). Barrau et al. observed the worst performance with no liquid flow and/or at low gas fractions.
- *Bubble rise velocity.* The rise time errors are primarily affected by the impact angle of the bubbles with the probe tip. The relative difference reported in the literature, compared with other techniques (i.e., image processing) are +45% (Cartellier and Barrau, 1998), +5% (Kiambi et al., 2003), between +5 and +6% (Chang et al., 2003), between +10 and +30% (Chaumat et al., 2005a), +15% (Simonnet et al., 2007), and +29% (Lima Neto et al., 2008), approximately +9% (Zhang and Zhu, 2013).
- *Bubble diameter.* The assumption of spherical bubbles leads to an underestimation of the equivalent diameter by between

+10% and 27% (Chaumat et al., 2005a; Lima Neto et al., 2008; Zhang and Zhu, 2013). Applying a correction based on the aspect ratio evaluation can reduce the error, e.g., from +26.6 to +7% (Zhang and Zhu, 2013).

2.5. Photography

2.5.1. Instrumentation

The photos were taken using a NIKON D5000 camera (f/3.5, 1/1600s, ISO400); the back light method is employed in the experiments using a 500 W halogen lamp as the light source. Visualization sections consist in squared boxes (filled with water) around the vertical pipe designed for correcting the distorted image (Fig. 2b). The camera was accurately aligned horizontally to the visualization sections. The resolution of each image is 4288×2848 pixels. Images have been acquired at approximately $h_{image}=2.4$ m and $h_{image}=1.4$ m from the sparger (developed region of the two-phase flow) and near the sparger.

2.5.2. Image analysis methods

The goal of the image analysis is to obtain bubble shape, bubble orientation and bubble size distributions. The image analysis method considers two types of bubbles: spherical/ellipsoidal bubbles (Fig. 4a) and distorted bubbles (i.e., near-sparger bubbles, Fig. 4b). Indeed, at the sparger, some bubbles were characterized by an ellipsoidal shape, and others by an irregular shape (i.e., due to the channeling effect (Hur et al., 2013)).

2.5.2.1. Image analysis method for spherical/ellipsoidal bubbles. For sampling the spherical/ellipsoidal bubbles, we use the same approach that we have successfully applied to a large-diameter annular-gap bubble column (Besagni et al., 2015; Besagni and Inzoli, 2016b). In this approach, each bubble is approximated and reconstructed using an ellipse (Fig. 4a), represented by the following equation:

$$c_1x^2+c_2xy+c_3y^2+c_4x+c_5x+1=0 \tag{15}$$

The method is structured in three phases:

1. *Calibration.* The reference conversion factor between pixels and millimeters is provided;
2. *Bubble reconstruction.* For each bubble, six points on the bubble are selected (by human vision), and ellipse equation parameters c_1, c_2, c_3, c_4 and c_5 are evaluated using the least square method;
3. *Bubble processing.* The equivalent ellipse is processed to obtain the major axis $2a$, the minor axis $2b$, the center of the bubble and the orientation angle θ (Fig. 4a). Finally, the bubble equivalent diameter d_{eq} and aspect ratio φ are obtained:

$$d_{eq}=2\sqrt{a^2b} \tag{16}$$

$$\varphi=\frac{b}{a} \tag{17}$$

Two references are used: a ruler inside the column and one along the external wall.

2.5.2.2. Image analysis method for distorted bubbles. Near the sparger, in addition to the spherical/ellipsoidal bubbles, some bubbles have an irregular shape, and some phenomena such as the channeling effect occur. The method for sampling the channeling/distorted bubbles (Fig. 4b) is structured in three phases:

1. *Calibration.* The reference conversion factor between pixels and millimeters is provided;
2. *Bubble reconstruction.* For each bubble, several points on the bubble edge are selected (by human vision), and a fitting line is obtained by using the least square method;
3. *Bubble processing.* The symmetry axis is evaluated and, using the hypothesis of the axi-symmetric bubble, the bubble equivalent diameter d_{eq} is obtained.

The reference length is the sparger itself.

2.5.3. Bubble sampling

The number of bubbles to be sampled to achieve a reliable BSD is a matter of discussion in the literature (Honkanen et al., 2005). Various studies have sampled different numbers of bubbles—between 50 and 100 (Lage and Espósito, 1999), 200 (Wongsuchoto et al., 2003), 250 (Rakoczy and Masiuk, 2009), 300 (Hanselmann and Windhab, 1998), between 250 and 300 (Aloufi, 2011) and 100 (Passos et al., 2015). In this study, for each case, at least 800 bubbles were selected using two (or more) photos. Using image analysis, five superficial gas velocities have been analyzed in the batch ($U_L=0$ m/s) and counter-current mode ($U_L=-0.066$ m/s). The image analysis is applied for studying the developed and sparger regions. For a complete discussion considering the uncertainties of the image analysis the reader should refer to Besagni and Inzoli (2016b).

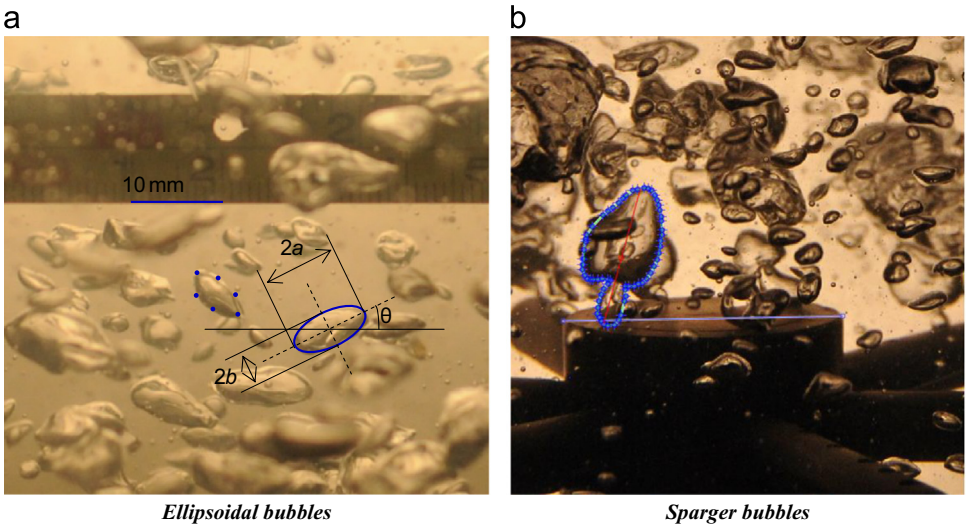

Fig. 4. Image processing.

3. The experimental results

3.1. Holdup

3.1.1. Holdup measurements

Fig. 5 displays the holdup measurements. At low air superficial velocity, in the homogeneous regime (Fig. 6a), the relationship between the holdup and the air superficial velocity is linear, followed by a change in slope due to the regime transition (Fig. 6b and c) toward the transition regime (Fig. 6d–f). The slug flow was not observed, which agrees with the Shah flow map (Shah et al., 1982) and the large-diameter theory (Section 1). Following the discussion proposed by Nedeltchev (Nedeltchev and Schubert, 2015), the homogeneous regime—in the present bubble column—can be regarded as a maldistribution regime owing to the large sparger openings, d_o. The drift flux plots (Section 3.2), flow visualizations (Section 3.3) and optical probe measurements (Section 3.4) confirm the existence of the maldistribution regime. For the sake of clarity, in the following, we simply refer to the homogeneous regime. The shape of the holdup curve is the one typically found for similar sparger geometries: the shape of the holdup curve mainly depends upon the sparger used and its openings (Urseanu, 2000). The sparger used in this study has "*large*" holes ($d_0 > 1$ mm), and the shape of the holdup curve is the one typically obtained for a sparger with similar hole openings (i.e., single/multiple nozzles, spider sparger or perforated plate sparger with a hole diameter greater than 1 mm); as expected, no peak can be observed in the holdup curve. Alternatively, when using "*fine*" spargers, a peak in the holdup curve may appear, as obtained by Al-Oufi (Al-Oufi et al., 2010, 2011), Schumpe and Grund (1986), and Zahradnik et al. (1997).

Upon increasing the liquid flowrate, a faster increase in the holdup is observed at low U_G, and the transition point also moves toward lower superficial gas velocities (Section 3.2). This change is explained by the effect of the liquid flow, which slows down the rise of the bubbles, leading to higher holdup: the more compact arrangement of the bubbles leads to an earlier flow regime transition (Sections 3.2 and 3.4). Our results prove that U_L (counter-current mode) has an influence on the holdup, which agrees with the findings of Otake et al. (1981), Baawain et al. (2007), Biń et al. (2001), Jin et al. (2010), Besagni et al. (2014, 2015) and Besagni and Inzoli (2016a) but disagrees with Akita and Yoshida (1973). Our results are probably due to the comparable order of magnitude of the liquid and gas velocities. Hills (1976) mentioned that if U_L is low compared with the bubble rise velocities, no impact of the liquid velocity on holdup is expected because the acceleration of the bubbles will be negligible. This hypothesis is confirmed by using the approach of Rollbusch et al. (2015a): the bubble swarm velocities (Section 3.2) are comparable with the liquid velocities.

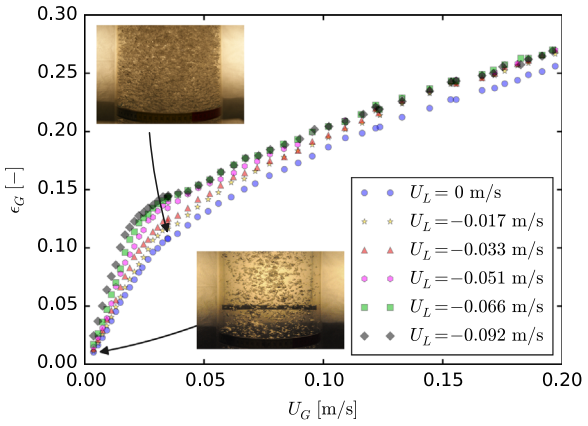

Fig. 5. Holdup measurements.

Above the transition velocity, large, deformed bubbles begin to appear (Fig. 6d–f), and the bubble coalescence increases the average rise velocity and reduces the gas residence time in the column, thus reducing the holdup versus gas velocity slope. In this region, the slope of the curve changes continuously, indicating a continuous increase of the "*coalescence-induced*" bubble component (Urseanu, 2000). In this regime, large periodic eddies accompanied with flow recirculation are observed all along the vertical development of the pipe. This is further discussed in the next paragraph (gas disengagement technique) and in Section 3.4 (optical probe). Above a certain holdup (depending on U_L), the liquid superficial velocity has no more influence on the holdup. A similar behavior was observed by Besagni et al. (2014, 2015) while studying an annular gap "*AG*" bubble column equipped with a pipe sparger (Fig. 7). The main difference between the present bubble column and the "*AG*" bubble column is the value of the holdup for which U_L has no more influence. In the literature, Jin et al. (2010) observed that the influence of working mode is lower at high holdup. The discrepancy of the holdup in the transition regime between the batch and counter-current modes is hardly justified. This behavior was also discussed by Besagni et al. (2014, 2015)—for the "*AG*" bubble column—where the proposed cause was the asymmetric distributor, which generated a larger flow development zone in the no-liquid flow configuration with respect to the counter-current cases, owing to the lower liquid back-mixing. Besagni and Inzoli (2016a) also studied the influence of the inner pipes on the "*AG*" configuration: the inner tubes were removed, and the results for the open tube "*OT*" bubble column are displayed in Fig. 8. As the reader can observe, the liquid velocity has a continuous influence on the holdup value. The asymmetrical injection without the inner pipes may cause this behavior. Our results suggest the hypothesis that the influence of the counter-current mode on the holdup depends upon the column design (which also applies to large-diameter columns). It is worth noting that the "*spider-sparger*" holdup curves obtained in this study are similar to the holdup curves obtained using the same experimental facility equipped with the "*pipe-sparger*" in the "AG" and "OT" configurations (Section 3.1.2.2). This suggests a limited influence of the sparger design in large-diameter bubble columns, possibly due to the large-diameter and the sparger with large openings. This concept was also discussed in the experimental investigation proposed by Besagni and Inzoli (Besagni and Inzoli, 2016a).

The hydrodynamics of the column and the structure of the holdup are further investigated using the GD technique, and the results are presented in Fig. 9 along with the results of Schumpe and Grund (1986) (d_c=0.3 m, H_c=4.4 m). The holdup values and the holdup of the "*non-coalescence-induced*" and the "*coalescence-induced*" bubble classes are plotted in Fig. 9a: the holdup measured by the bed expansion technique and the GD technique are in good agreement. The mean rise velocity and the holdup of the "*non-coalescence-induced*" and the "*coalescence-induced*" bubble classes are plotted in Fig. 9a. "*Coalescence-induced*" bubbles begin to form at approximately U_G=0.03 m/s, which corresponds approximately to the end of the homogeneous regime (this is verified in the next section). The rise velocity of the large bubble class increases with increasing gas flowrate and their contribution to the total holdup. This indicates that the transition from the homogeneous regime is a gradual process. Similar results have been reported in the literature (Camarasa et al., 1999; Schumpe and Grund, 1986). Whereas the large bubble contribution increases with U_G, the small bubble rise velocity after an initial decrease remains constant at approximately 0.1–0.15 m/s. Beyond the regime transition, the holdup of the "*non-coalescence-induced*"

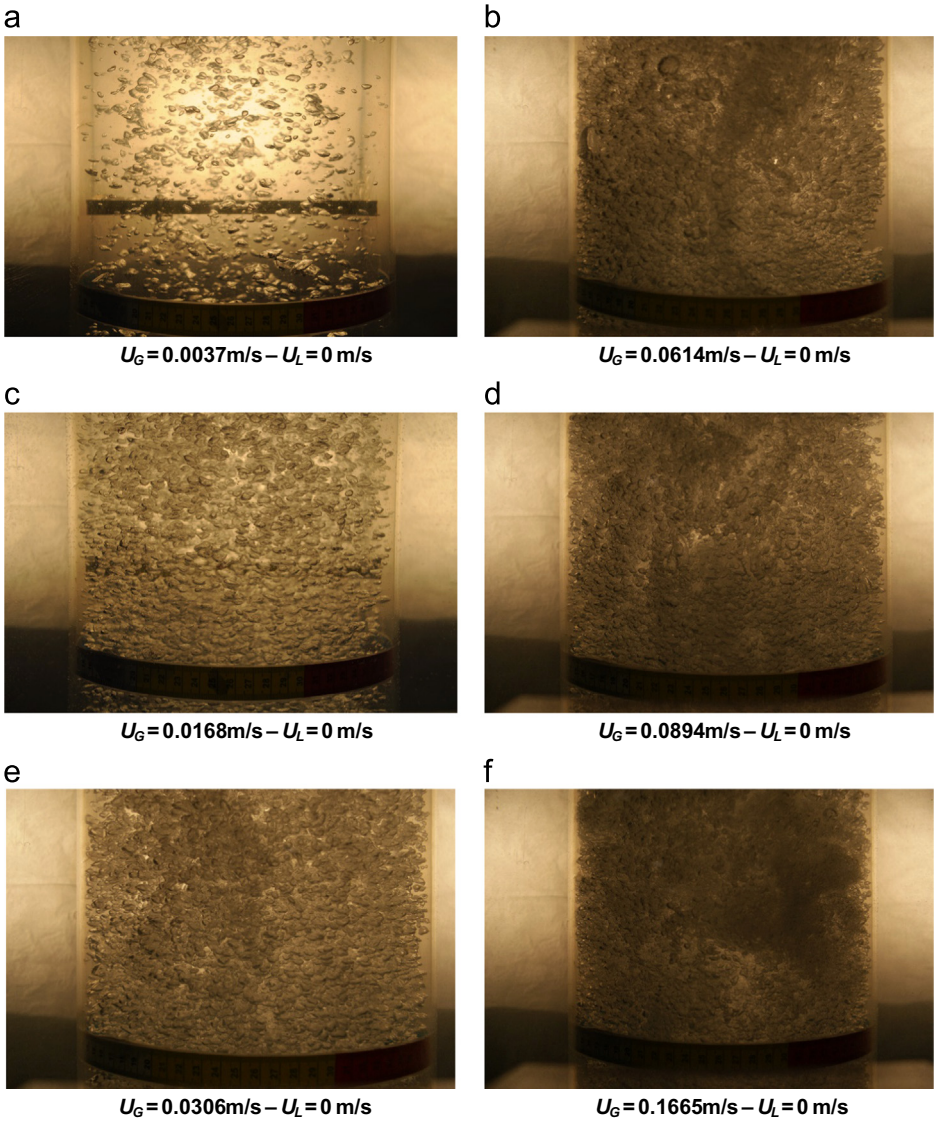

Fig. 6. Photographs of the air–water flow at $h = 2.4$ m from the sparger: influence of U_G.

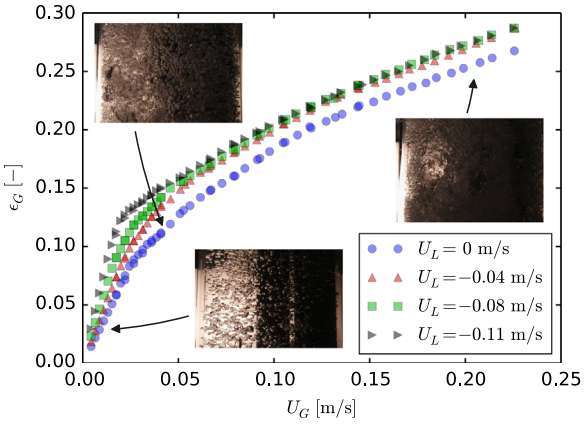

Fig. 7. Holdup measurements in the annular gap (AG) configuration – Besagni et al. (2014, 2015).

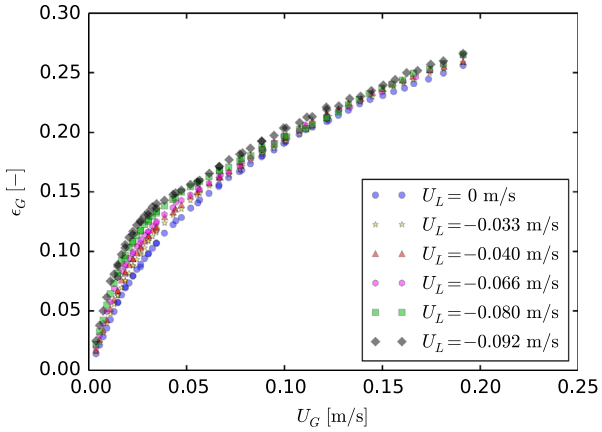

Fig. 8. Holdup measurements in the open tube (OT) configuration – Besagni and Inzoli (2016a).

bubble increases only slightly, and so the augmentation of the total holdup is mainly due to the increase in the holdup of fast-rising "*coalescence-induced*" bubbles. It should be noted that if holdup values measured by the bed expansion and the GD technique are in good agreement, the rise velocities of large bubbles obtained by GD are overestimated compared with terminal rising velocities of "*coalescence-induced*" bubbles because of the presence of internal liquid circulation (Camarasa et al., 1999; Deshpande et al., 1995). Our results agree with the findings of Schumpe and Grund (1986),

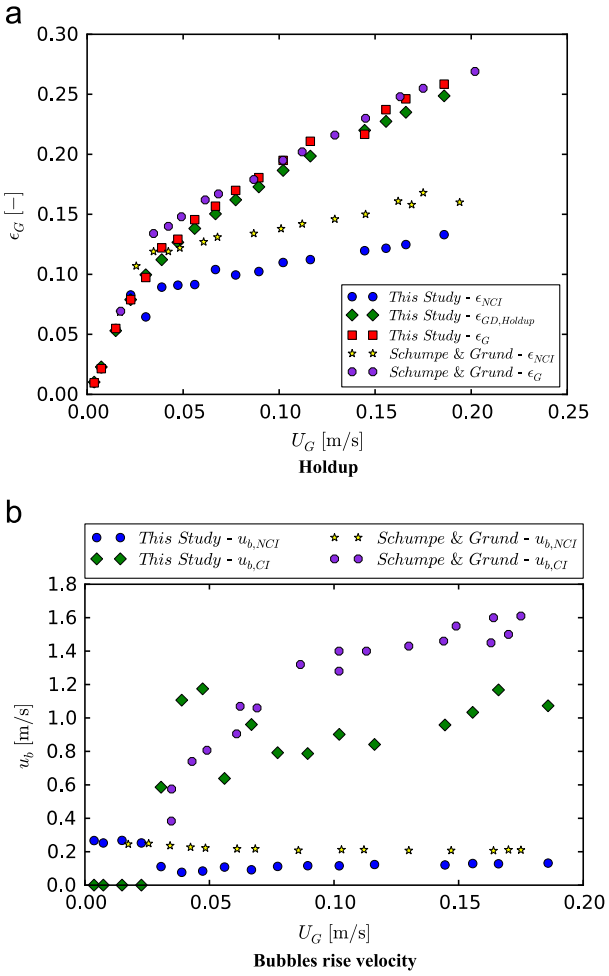

Fig. 9. Gas disengagement results.

except for the transition point: in this case, the homogeneous regime is destabilized earlier (refer to the next section for further details) and the contribution of the "*non-coalescence-induced*" bubbles to the overall holdup is lower compared with that found by Schumpe and Grund (1986).

3.1.2. Comparison with data from the literature

In the literature, several experimental data are available on bubble columns. Herein, we compare our results (in the batch mode) with a set of experimental studies with similar column diameters and sparger designs (Akita and Yoshida, 1973; Besagni et al., 2015; Fair et al., 1962; Gopal and Sharma, 1983; Kawase and Moo-Young, 1987a; Otake et al., 1981; Reilly et al., 1986; Sada et al., 1984; Schumpe and Grund, 1986; Thorat et al., 1998; Ying et al., 1981; Yoshida and Akita, 1965). At first, we compare the data in the low U_G range (Fig. 10, Table 1), and then we compare the data in the complete U_G range (Fig. 11, Table 2). When comparing holdup data between different configurations—at the same operating conditions (i.e., atmospheric pressure and temperature)—some design parameters must be considered (Rollbusch et al., 2015a):

- *Column diameter* (or, if the operating conditions are fixed, the non-dimensional diameter, Eq. (1)). Despite some contradictory results, it appears that column size d_c=0.15 m is sufficiently large to obtain holdup values that can be used to predict holdup in larger columns (Kantarci et al., 2005);
- *Sparger openings.* The role of the sparger opening was already discussed in Section 3.1.1;

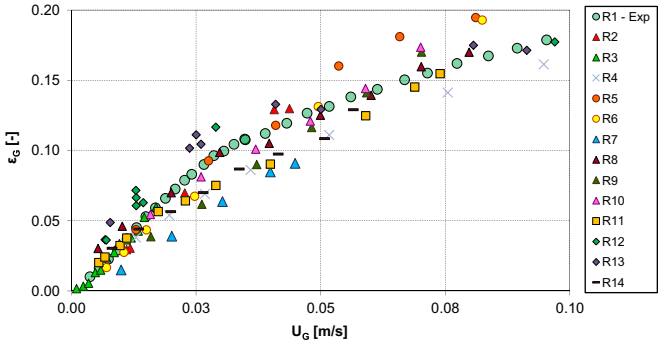

Fig. 10. Holdup measurements – Comparison between the experimental results and the data from the literature: low superficial gas velocity range.

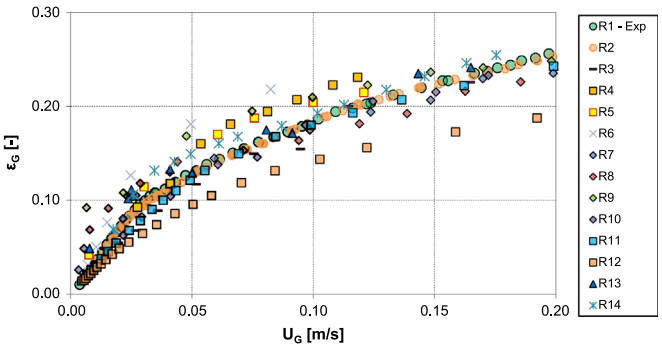

Fig. 11. Holdup measurements – comparison between the experimental results and the data from the literature: complete gas velocity range.

Table 1
Literature studies and code reference to Fig. 10.

Code	Reference	d_c [m]	Aspect ratio [dimensionless]	Sparger
R1 – Exp.	This study	0.24	22.1	Spider sparger d_0=1–3.5 mm
R2	Fair et al. (1962)	0.46	6.63	Ring Sparger d_0=0.5 mm
R3	Fair et al. (1962)	1.07	2.85	Ring Sparger d_0=0.76 mm
R4	Akita and Yoshida (1973)	0.152	26.32	Single hole d_0=5 mm
R5	Otake et al. (1981)	0.05	30	Single nozzle d_0=5 5 mm
R6	Otake et al. (1981)	0.05	30	Multiple nozzle d_0=0.65 mm
R7	Gopal and Sharma (1983)	0.2	4	Single Nozzle d_0=6 mm
R8	Gopal and Sharma (1983)	0.2	4	Ring Sparger d_0=1 mm
R9	Gopal and Sharma (1983)	0.6	1	Ring Sparger d_0=2 mm
R10	Gopal and Sharma (1983)	0.6	1	Ring Sparger d_0=3 mm
R11	Sada et al. (1984)	0.073	13	Single Nozzle d_0=1.5 – 2.7 – 5.7 mm
R12	Reilly et al. (1986)	0.3	16.7	Perforated plate d_0=1.5 mm
R13	Reilly et al., (1986)	0.3	16.7	Single Sparger d_0=25.4 mm
R14	Kawase and Moo-Young (1987a)	0.23	5.3	Multiple nozzle d_0=1 mm

- *Aspect ratio.* In systems where the bubble sizes are not at their maximum equilibrium size, the holdup would decrease with increasing liquid height: the longer the column, the more time the bubbles have to coalesce. This is confirmed by, for example,

Table 2
Literature studies and code reference to Fig. 11

Code	Reference	d_c [m]	Aspect ratio [dimensionless]	Sparger
R1 – Exp.	This study	0.24	22.1	Spider sparger d_0=1–3.5 mm
R2	Besagni et al. (2015)	0.24 Annular gap	22.1	Pipe Sparger d_0=3.5 mm
R3	Akita and Yoshida (1973)	0.152	26.32	Single hole d_0=5 mm
R4	Ying et al. (1981)	0.305	–	Single hole d_0=1.66 mm
R5	Ying et al. (1981)	0.127	–	Single hole d_0=1.66 mm
R6	Otake et al. (1981)	0.05	30	Single nozzle d_0=5 5 mm
R7	Thorat et al. (1998)	0.385	7	Sieve Plate d_0=1 mm
R8	Thorat et al. (1998)	0.385	7	Sieve Plate d_0=1.5 mm
R9	Thorat et al. (1998)	0.385	7	Sieve Plate d_0=3.0 mm
R10	Thorat et al. (1998)	0.385	7	Sieve Plate d_0=6.0 mm
R11	Yoshida and Akita, 1965)	0.0707	12–33	Single nozzle d_0=2.25–7 mm
R12	Yoshida and Akita (1965)	0.30	4–6.3	Single nozzle d_0=1.48–3.00 mm
R13	Reilly et al. (1986)	0.3	16.7	Single Sparger d_0=25.4 mm
R14	Schumpe and Grund (1986)	0.3	12	Single Sparger d_0=1 mm

Ruzicka et al. (2001) and Voigt (Voigt and Schügerl, 1979). However, there seems to be no influence by the liquid height on the holdup for large aspect ratios, as reported by other investigators (Deckwer et al., 1980; Godbole et al., 1984; Hikita and Kikukawa, 1974). It is generally admitted that holdup is independent of aspect ratio for columns in which the aspect ratio is higher than 5 (Kantarci et al., 2005).

Another parameter that should be considered is the water quality, as stated by Kemoun et al. (2001) and remarked by Rollbusch et al. (2015a): if tap water is used, its qualities differ from location to location; if deionized water is used, the qualities may differ from day to day, and remnants of used liquids and dirt may be present and affect the results. The interested reader may refer to the discussion of Rollbusch et al. (2015a).

3.1.2.1. Low gas velocity range. Considering low gas velocities (Fig. 10, Table 1), our experimental measurements are in good agreement with the holdup data of Fair et al. (1962) (*R2* and *R3*) and Gopal and Sharma (1983) (*R8* and *R9*). The differences between the two set of data from Fair et al. (1962) (*R3* and *R4*) are in dc and the aspect ratio. Gopal and Sharma (1983) (*R7–R9*) studied bubble columns with low aspect ratios and different diameters and sparger openings; among the different datasets, *R8* (d_0=1 mm, d_C=0.2 m) and *R9* (d_0=2 mm, d_C=0.6 m), are in good agreement with our study. However, when considering larger (*R7*) or smaller (*R10*) openings, the holdup data are slightly different. The holdup curve of Sada et al. (1984) (*R11*), at low U_G, is quite agreeable with our study, probably because the homogeneous regime is provided by a sparger with a similar opening to the present study. The data of Akita and Yoshida (1973) (*R4*) are lower than our measurement, and the data of Otake et al. (1981) (*R5* and *R6*) agree with our measurement only up to U_G=0.05 m/s. Finally, the data of Reilly et al. (1986) (*R12* and *R13*) and that of Kawase and Moo-Young (1987a) (*R14*) are comparable with our dataset: the former has higher holdup values, and the latter has lower.

3.1.2.2. Complete operating range. Considering the complete U_G range (Fig. 11, Table 2), our experimental measurements are in good agreement with the holdup data of the AG bubble column of Besagni et al. (2015) (*R2*) and the data of Yoshida et al. (Yoshida and Akita, 1965) (*R11*), Reilly et al. (1986) (*R13*) and Schumpe and Grund (1986) (*R14*). The "*AG*" bubble column configuration studied by Besagni et al. (2015) (*R2*) was obtained in this same facility but using inner pipes: the data are in very good agreement; further details may be found in Section 3.1.1. In addition, our data are in good agreement with the "*OT*" configuration studied by Besagni and Inzoli (Section 3.1.1). The holdup data of Akita and Yoshida (1973) (*R3*) are lower than our measurements; the data of Ying et al. (1981) (*R4* and *R5*) either overestimate or underestimate our data, but no information is available for the column height, so no conclusion may be drawn for this configuration. The measurements of Otake et al. (1981) (*R6*) are higher compared with our data. The holdup data of Thorat et al. (1998) (*R7–R10*) are in good agreement with our measurements, except for the *R9* configuration. Concerning the study of Yoshida et al. (Yoshida and Akita, 1965) (*R11* and *R12*), the dataset *R11* is in very good agreement with our data, and the dataset *R12* has a lower holdup (owing to the lower aspect ratio). Finally, the data of Reilly et al. (1986) (R13) and the data of Schumpe and Grund (1986) (*R14*) are comparable with our dataset.

3.1.3. Comparison with correlation from the literature

Many correlations have been proposed in the literature for the holdup. Herein, a set of correlations have been selected and compared with our data (Fig. 12):

- Hughmark (1967):

$$\varepsilon_G = \frac{1}{2+\left(\frac{0.35}{U_G}\right)\left[\frac{\rho_L \sigma}{72}\right]^{1/3}} \tag{18}$$

- Mashelkar (1970):

$$\varepsilon_G = \frac{U_G}{0.3+2\cdot U_G} \tag{19}$$

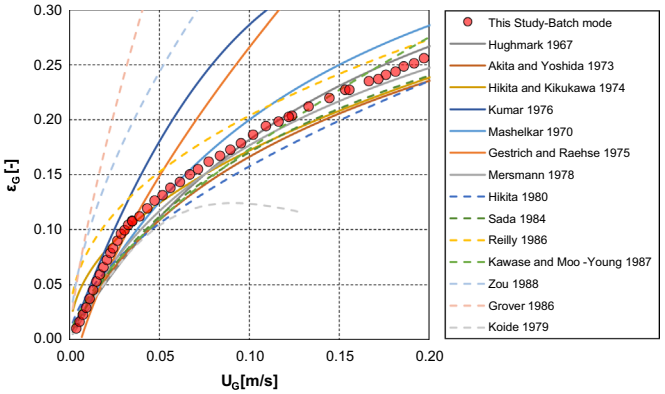

Fig. 12. Holdup measurements – comparison between the experimental results and correlations from the literature.

- Akita and Yoshida (1973):

$$\frac{\varepsilon_G}{(1-\varepsilon_G)^4} = c_1 \left(\frac{g{d_c}^2 \rho_L}{\sigma}\right)^{1/8} \left(\frac{g{d_c}^3}{{\nu_L}^2}\right)^{1/12} \left(\frac{U_G}{\sqrt{g d_c}}\right) \tag{20}$$

- Hikita and Kikukawa (1974):

$$\varepsilon_G = 0.505 \cdot {U_G}^{0.47} \left(\frac{72}{\sigma}\right)^{2/3} \left(\frac{1}{\mu_L}\right)^{0.05} \tag{21}$$

- Sada et al. (1984):

$$\frac{\varepsilon_G}{(1-\varepsilon_G)^4} = 0.32 \cdot \left(\frac{g{d_c}^2 \rho_L}{\sigma}\right)^{0.121} \left(\frac{g{d_c}^3}{{\nu_L}^2}\right)^{0.086} \left(\frac{U_G}{\sqrt{g d_c}}\right) \left(\frac{\rho_G}{\rho_L}\right)^{0.068} \tag{22}$$

- Reilly et al. (1986):

$$\varepsilon_G = 296 \cdot {U_G}^{0.44} {\rho_L}^{-0.98} \sigma^{-0.16} {\rho_G}^{0.19} + 0.009 \tag{23}$$

- Kawase and Moo-Young (1987b):

$$\varepsilon_G = 1.07 \cdot n^{2/3} \left(\frac{U_G^2}{g d_c}\right)^{1/3} \tag{24}$$

The experimental data (batch mode, $U_L = 0$ m/s) and the foregoing correlations are compared in Fig. 12. The reader should refer to Besagni and Inzoli (Besagni and Inzoli, 2016a) for a detailed discussion of these correlations and their range of applicability. The experimental data are well predicted for both low and high air superficial velocities by the correlation of Hughmark. The correlation of Reilly et al. reveals a similar trend to the experimental data; however, a constant shift in holdup is observed. The correlation of Kawase and Moo-Young underestimates the data in the homogeneous regime and overestimates the data in the churn turbulent flow regime. The correlation of Hikita and Kikukawa exhibits the opposite behavior. All of the other correlations underestimate the data in all of the flow regimes. These correlations have been obtained considering datasets obtained in different experimental setups. The holdup is a function of the column design and operation, phase properties (both liquid and gas) and operating conditions. Therefore, the discrepancies between these correlation and the present dataset depend on the different column design, sparger (i.e., the maldistribution at the sparger) and operating conditions (ambient temperature and pressure).

3.1.4. *Proposed correlations for the holdup*

The correlations from the literature have low accuracy in predicting the holdup throughout the operating range; therefore, a new correlation is proposed following the same approach that we have successfully applied in our previous papers (Besagni et al., 2015; Besagni and Inzoli, 2016a). The correlation is based on our data in the batch mode only and will be extended to the counter-current mode in future works. The relationship between the holdup and the physical properties of the system may be written as a function of the following parameters:

$$\varepsilon_G = f\left(g, U_G, d_{eq}, \mu_L, \rho_L - \rho_G, g\right) \tag{25}$$

This equation can be transformed through the dimensional analysis:

$$\varphi = f\left(\frac{U_G \mu_L}{\sigma}, \frac{g\,\mu_L^4}{(\rho_L - \rho_G)\,\sigma^3}\right) = f(Ca, Mo) \tag{26}$$

Different formulations can be used for the function *f*, and, in this paper, the same expression proposed by Akita and Yoshida (1973) is used:

$$\frac{\varepsilon_G}{(1-\varepsilon_G)^n} = k_1\, Mo^{k_2} Ca^{k_3} \tag{27}$$

Holding the liquid properties constant, the Mo^{k2} term becomes constant:

$$\frac{\varepsilon_G}{(1-\varepsilon_G)^n} = k_1^*\, Ca^{k_3} \tag{28}$$

which can be rewritten as follows:

$$\ln\left(\frac{\varepsilon_G}{(1-\varepsilon_G)^n}\right) = k_3 \ln(Ca) + \ln(k_1^*) \tag{29}$$

which is equivalent to

$$y = m\,x + q \tag{30}$$

where $k_3 = \mathrm{m}$, $\ln(\mathrm{Ca}) = x$ and $\ln(k_1^*) = q$. The resulting correlation is:

$$\frac{\varepsilon_G}{(1-\varepsilon_G)^n} = 329.31\, Ca^{0.997} \tag{31}$$

Then, the exponent n is selected. Using $n = 4$, such as in Akita and Yoshida (1973), gives unsatisfactory results, and $n = 4.9$ is selected using a least square minimization method. The results are displayed in Fig. 13: the proposed correlation matches the data fairly well compared to the previous correlations in the literature. This correlation, obviously, may fit literature data reported in Figs. 10 and 11. The same comments as before also apply here and will not be repeated. In future studies, our experimental facility should be used for studying the influence of the liquid phase (i.e. viscous and "*non-coalescing*" solutions) over the holdup for proposing a new correlation for the gas holdup (also considering the literature data). For example, recently, Besagni and Inzoli (2015) recently studied the influence of electrolyte concentration over holdup, flow regime transition and local flow properties. In future study, the liquid velocity may be considered in the correlation development.

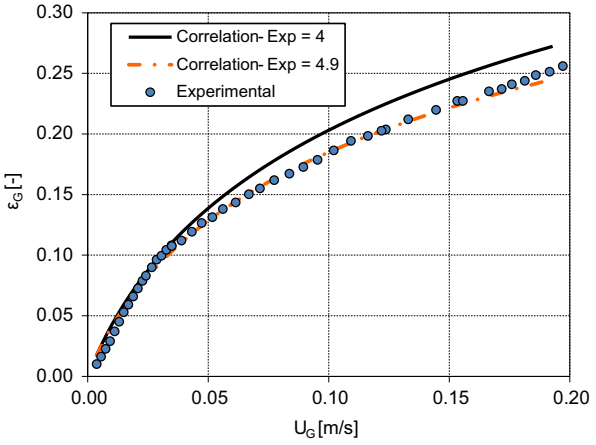

Fig. 13. Proposed correlation for the holdup in the batch mode ($U_L = 0$ m/s).

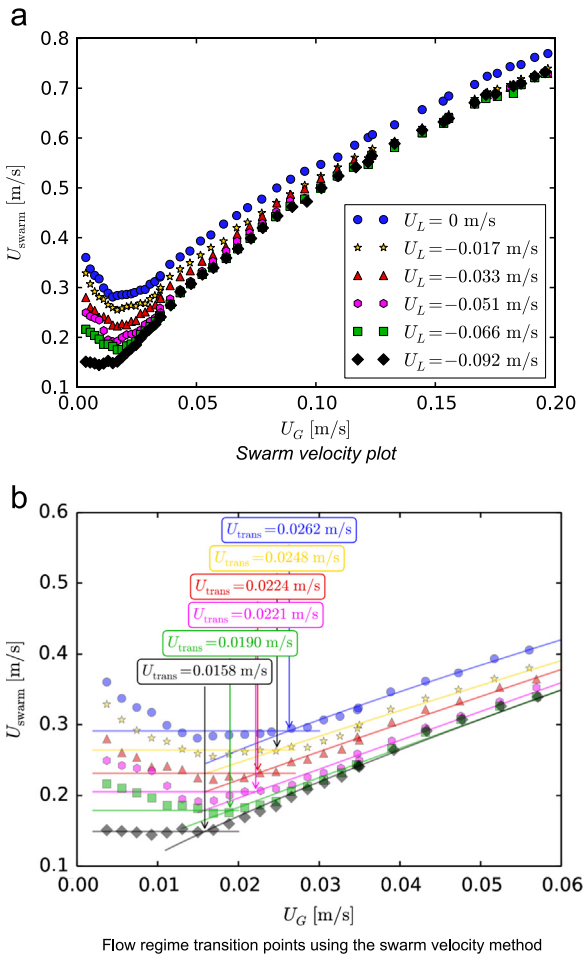

Fig. 14. Flow regime transition points: the swarm velocity method.

3.2. Flow regime transition

The results of the swarm velocity (Section 2.2.2.1) and the drift flux method (Section 2.2.2.2) are displayed in Figs. 14 and 15, respectively. The transition points agree between the two methods, and following the proposal of Ribeiro Jr and Mewes (2007) and Besagni and Inzoli (2015), the transitional holdups and gas velocities are evaluated as the mean of the two values. The transition points are displayed in Fig. 16 along with the transition points of the "*AG*" (Fig. 7; Besagni et al., 2014, 2015) and the "*OT*" (Fig. 8; Besagni and Inzoli, 2016a) configurations. The counter-current mode destabilizes the homogeneous regime (U_{trans} decreases with increasing U_L). Indeed, the counter-current liquid slows the bubbles and increases the holdup (Fig. 5), the local void fraction and the bubble mean diameter (Section 3.4): for the same U_G, the mean distance between the bubbles decreases, and coalescence phenomena may occur more easily because of the expected increase in the bubble collisions. In the present configuration, U_{trans}, depending on U_L, lies between 0.0264 m/s and 0.0173 m/s. In the batch mode, the transition points of the present bubble column and the "*AG*" bubble column are close. Krishna et al. (2000) suggested that similar transition points indicate similar column hydrodynamics, and as discussed before, the present bubble column has a similar behavior to the "*AG*" bubble column. Alternatively, in the "*OT*" bubble column, the regime transition begins earlier, and this configuration also has different hydrodynamic behavior (as discussed before). A possible cause for the earlier regime transition in the "*OT*" bubble column may be the sparger, which causes higher bubble coalescence in the region upstream of itself owing to the absence of the inner pipes. In the literature, Otake et al. (1981) observed an increase in the holdup and earlier regime transitions with increasing counter-current liquid flowrate in a small pipe of diameter 0.05 m. Their analysis covered gas superficial velocities up to 0.0824 m/s and liquid superficial velocities up to −0.15 m/s. Similar conclusions were drawn by Yamaguchi and Yamazaki (1982b) for small pipes of diameters 0.04 m and 0.08 m, with gas superficial velocities up to −1 m/s. In contrast, Akita and Yoshida (1973) observed that the liquid flowrate had no influence in a large pipe with a diameter 0.152 m at gas superficial velocities up to 0.032 m/s and liquid superficial velocities up to −0.04 m/s. The latter disagrees with what we observed in the homogeneous regime, whereas the former suggests an influence of liquid flowrate at gas superficial velocities higher than 0.06 m/s. Our results, considering the literature, support the idea of a correlation between the superficial liquid velocity and the transitional velocity.

Focusing on the batch mode, the typical values of U_{trans} found in the literature for air–water systems in bubble columns of diameter greater than 0.15 m range between 0.01 and 0.08 m/s under ambient operating conditions (Dargar and Macchi, 2006; Hur et al., 2013; Krishna et al., 1991; Letzel et al., 1999; Reilly et al., 1994; Ruzicka et al., 2001; Schumpe and Grund, 1986; Urseanu, 2000; Wilkinson et al., 1992; Zahradnik et al., 1997). The value depends mainly on the sparger type. Single and multiple nozzles or perforated plate spargers with a hole diameter greater than 1 mm ("*coarse*" spargers) usually lead to an early regime transition, whereas "*fine*" spargers such as porous plates (Al-Oufi et al., 2010, 2011) or needles (Mudde et al., 2009) can maintain a stable homogeneous regime at higher gas flowrates (i.e., Mudde et al. (2009) reported a homogeneous regime up to a holdup equal to 0.55). The sparger considered in this study is of the "*coarse*" type, and the values of U_{trans} agree with the data and observations presented in the literature (i.e., the study of Dargar and Macchi (2006) and Rollbusch et al. (2015a)). A brief comparison with some of the previous studies is presented in Table 3. Ribeiro Jr and Mewes, Zahradnik et al. and Al-Oufi et al. reported a flow regime transition for a larger holdup than our value. Probably, this is due to the air distribution at the inlet (i.e., the porous sparger in Al-Oufi et al. or perforated plate sparger with $d_o < 1$ mm). The transition holdups measured by Krishna et al. and Urseanu and Letzel et al. are approximately 10% higher than those obtained in this study. This point was also discussed by Rollbusch et al. (2015a). The higher transition velocities and holdups in these studies can be explained considering the column diameter: the studies considered from the literature were carried out in columns with a small pipe diameter. Ruzicka et al. (2001) calculated U_{trans} in three bubble columns (d_c=0.14, 0.29, and 0.4 m) and found that an increase in d_c reduced transition velocity. Their results are also consistent with the observations of Zahradnik et al. (1997). Despite the fact that the experimental data lie within the ranges observed in the literature, the flow regime transition occurs quite early. This is probably due to the sparger used and the maldistribution regime. The maldistribution regime is verified here because the experimental data do not perfectly match the theoretical curve in the drift flux plots (Fig. 15).

Finally, we compare out experimental data with literature correlations. One of the first correlations was proposed by Wilkinson et al. (1992):

$$U_{trans} = 0.5 U_{b,small} \exp\left(-193 \rho_G^{-0.61} \mu_L^{0.5} \sigma^{0.11}\right) \quad (32)$$

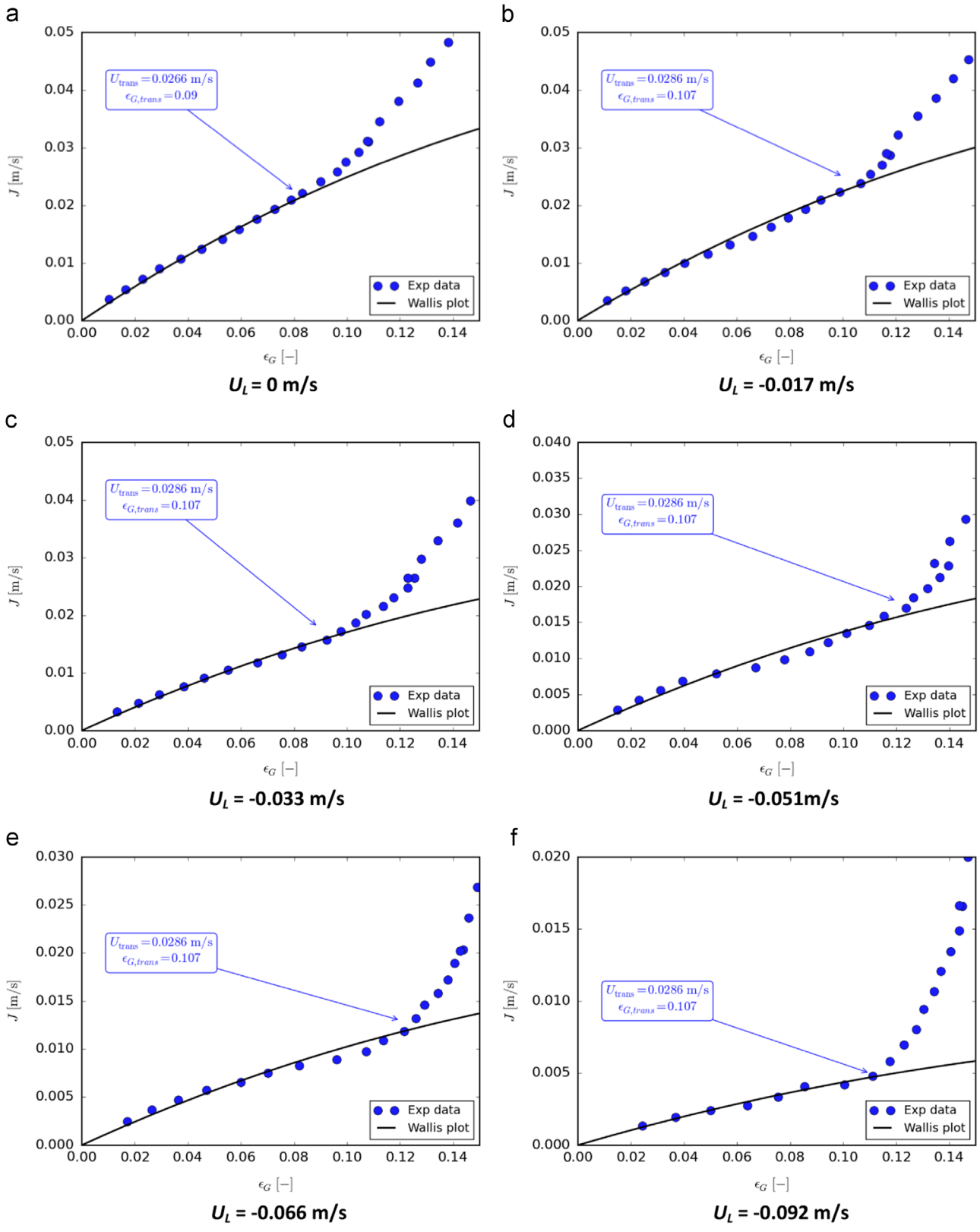

Fig. 15. Flow regime transition points: the drift flux method.

with

$$U_{b,small} = 2.25\frac{\sigma}{\mu_L}\left(\frac{\sigma^3\rho_L}{g\mu_L^4}\right)^{-0.273}\left(\frac{\rho_L}{\rho_G}\right)^{0.03} \tag{33}$$

Another correlation was proposed by Reilly et al. (1994) and reads:

$$U_{trans} = \frac{\rho_L}{\rho_G}(1-\varepsilon_{G,trans})\left(\frac{B^*}{A^*}\right)^{1.5} \tag{34}$$

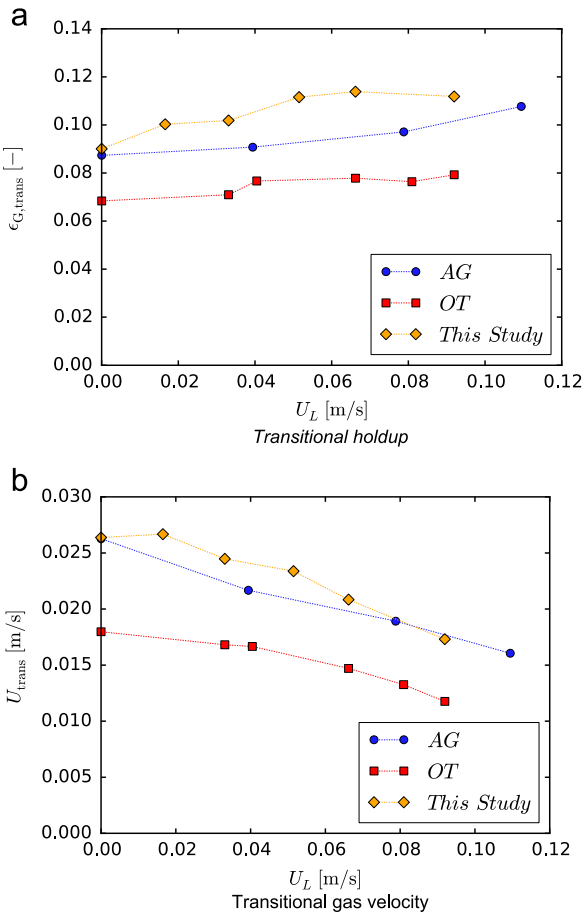

Fig. 16. Transition holdup and gas velocity: influence of the liquid velocity.

with, the holdup at the transition:

$$\epsilon_{G,trans} = 0.59 B^{*1.5} \left(\frac{\sigma^{0.12} \rho_G^{0.96}}{\rho_L} \right)^{0.5} \tag{35}$$

and:

$$A^* = 2.81 \rho_L \rho_G^{0.96} \sigma^{-0.12} \tag{36}$$

For water as the liquid phase, $B^*=4$. Comparisons of U_{trans} and $\epsilon_{G,trans}$ from the experimental investigation and these correlations are given in Table 4. Eq. (25) largely underestimates the transition gas velocity. This observation was also made by Letzel et al. (1999), who also compared their results with the correlation of Reilly et al. (1994), which provide a better agreement. On the other hand, Eq. (27) gives a value for U_{trans} and $\epsilon_{G,trans}$ in agreement with the experimental data.

3.3. Image analysis

The image analysis is applied for five U_G values between $U_G=0.0037$ m/s and $U_G=0.0188$ m/s in the batch mode ($U_L=0$ m/s, $U_{trans}=0.0264$ m/s, ϵ_G between 1.02% and 6.60%, Fig. 17) and the counter-current mode ($U_L=-0.066$ m/s, $U_{trans}=0.0201$ m/s, ϵ_G between 1.02% and 8.00%, Fig. 18). Both the developed region and the sparger region were analyzed (Figs. 17 and 18). In the batch mode, the bubbles were sampled both in the center and near the wall of the column at $U_G=0.0037$ m/s (Fig. 17a) and $U_G=0074$ m/s (Fig. 17b). For higher U_G, the bubble overlap is such that sampling in the center of the column was impossible.

Table 3
Flow regime transition: comparison with data from the literature.

Reference	d_c [m]	Sparger type	$\epsilon_{G,trans}$ [dimensionless]	U_{trans} [m/s]
This study	0.24	Spider sparger d_o=1–4 mm	0.09	0.0264
Besagni and Inzoli, (2016a)	0.24	Pipe sparger d_o=3.5 mm	0.0683	0.0179
Besagni et al. (2014, 2015) and Besagni and Inzoli (2015)	0.24	Pipe sparger d_o=3.5 mm Annular gap	0.0874	0.0263
Zahradnik et al. (1997)	0.15	Perforated plate d_o=0.5 mm	0.21	0.04
Urseanu (2000)	0.051	Perforated plate d_o=0.5 mm	0.098	0.019
Urseanu (2000)	0.15	Perforated plate d_o=0.5 mm	0.127	0.027
Krishna et al. (2000)	0.15	Sieve plate d_o=0.5 mm	0.11	0.025
Letzel et al. (1999)	0.15	Perforated plate d_o=0.1 mm	0.13	0.027
Dargar and Macchi (2006)	0.152	Perforated plate d_o=0.8 mm	0.09	0.028
Ribeiro Jr and Mewes (2007)	0.12	Perforated plate d_o=0.7 mm	0.35	0.0405
Al-Oufi et al. (2011)	0.102	Porous sparger	0.26–0.15[a]	0.048–0.026[a]
Rollbusch et al. (2015a)	0.16	Perforated plate d_o=1 mm	0.068	0.03

[a] Depending on the geometrical configuration.

Table 4
Flow regime transition: comparison with correlations the literature.

	Exp.	Wilkinson et al. (1992)	Reilly et al. (1994)
U_{trans} [m/s]	0.0264	0.0029	0.0322
$\epsilon_{gas,trans}$ [dimensionless]	0.09[a]	0.011522[b]	0.1484

[a] The value is given by U_{trans}/U_{swarm}.
[b] The value is given by $U_{trans}/U_{b,small}$.

3.3.1. Developed region

3.3.1.1. Bubble size distributions. The bubble diameter distribution is detailed by using histograms with 26 classes (each class has an extension of 0.5 mm). Figs. 19a and 20a display the BSDs at the wall and at the center of the column for $U_G=0.0037$ m/s and $U_G=0.0074$ m/s, respectively. Near the wall, there is a higher number of small bubbles: this may be because of the lift force, which pushed the small bubbles toward the wall (Besagni and Inzoli, 2016b). It is well-known that the direction of the transversal lift force depends upon the bubble size and shape. For "*small bubbles*", the lift force acts in the direction of decreasing liquid velocity (i.e. batch or co-current mode, thus, the lift force pushes the small bubbles toward the wall), whilst for "*large bubbles*" it changes direction (a force that can be assimilated to the lift force tends to push large and deformed bubbles towards the center of the column (Lucas et al., 2005; Tomiyama et al., 2002)). This is also confirmed by the DNS studies of Santarelli and Fröhlich (2016). As a result, correlations for the lift coefficient usually display a change of sign from negative for "*small diameter*" ($d_{eq}<5.8$ mm for air–water at ambient condition) to positive for "*large bubbles*" ($d_{eq}>5.8$ mm for air–water at ambient condition). The change of sign of the lift coefficient is well described using the model of Tomiyama et al. (2002).

The BSDs near the wall are bimodal: the first peak of frequency appears between $d_{eq}=0.5$ mm and 1 mm, and the second is between $d_{eq}=3$ mm and 3.5 mm. In contrast, the BSDs at the center of the column are unimodal with a peak of frequency at

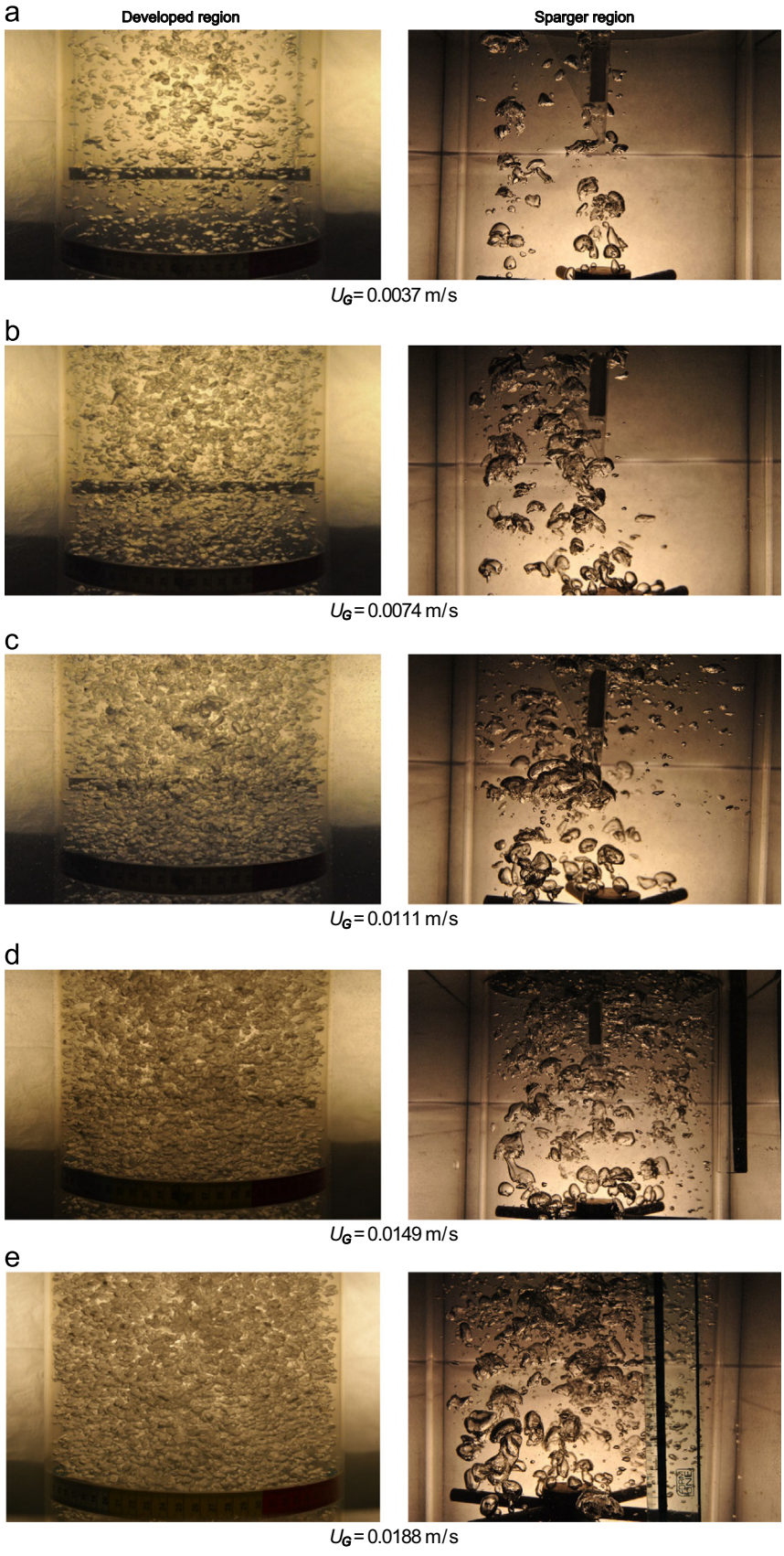

Fig. 17. Image analysis of the homogeneous regime: gas velocities investigated in the batch mode (U_L=0 m/s).

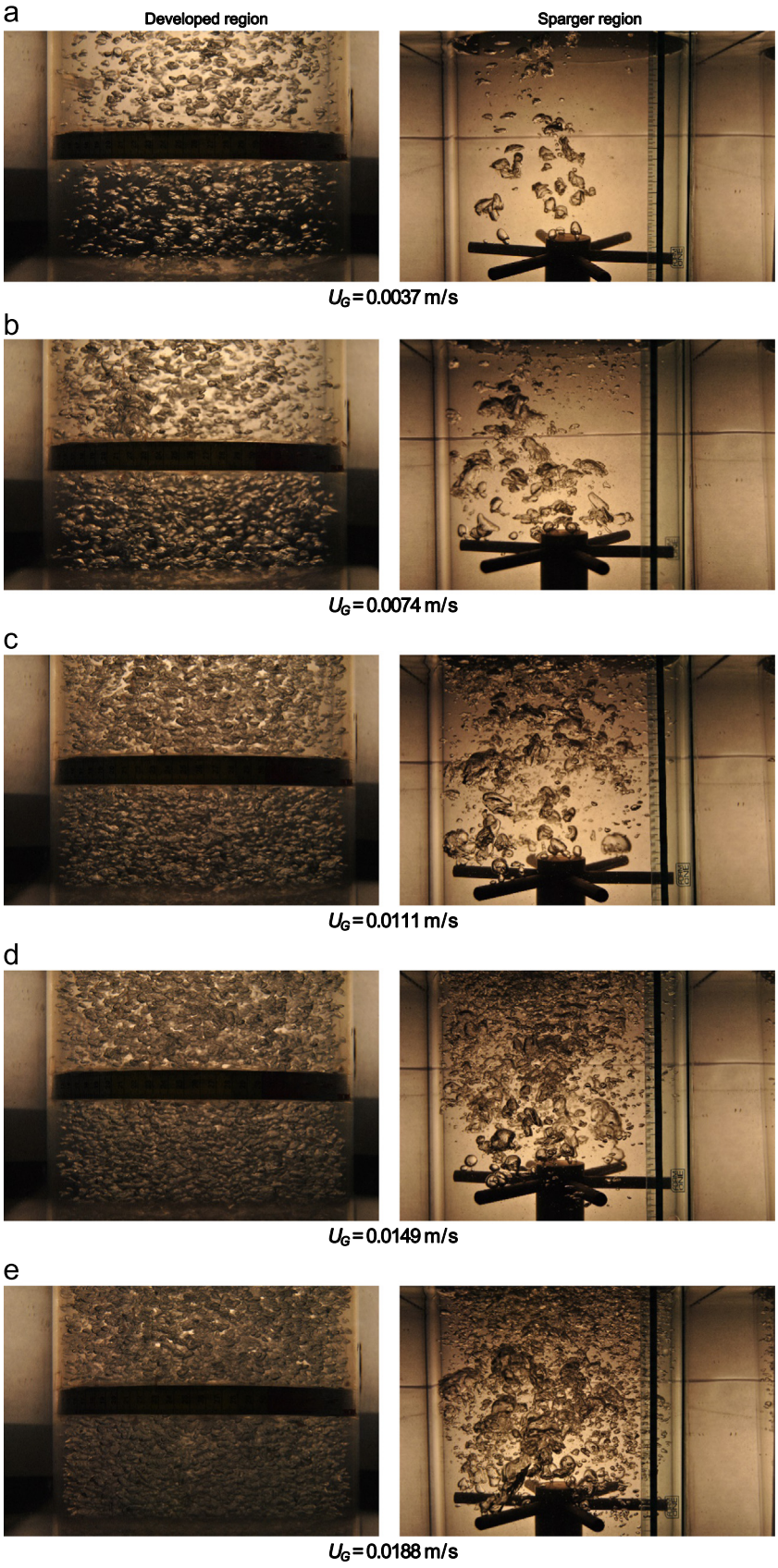

Fig. 18. Image analysis of the homogeneous regime: gas velocities investigated in the counter-current mode ($U_L = -0.06$ m/s).

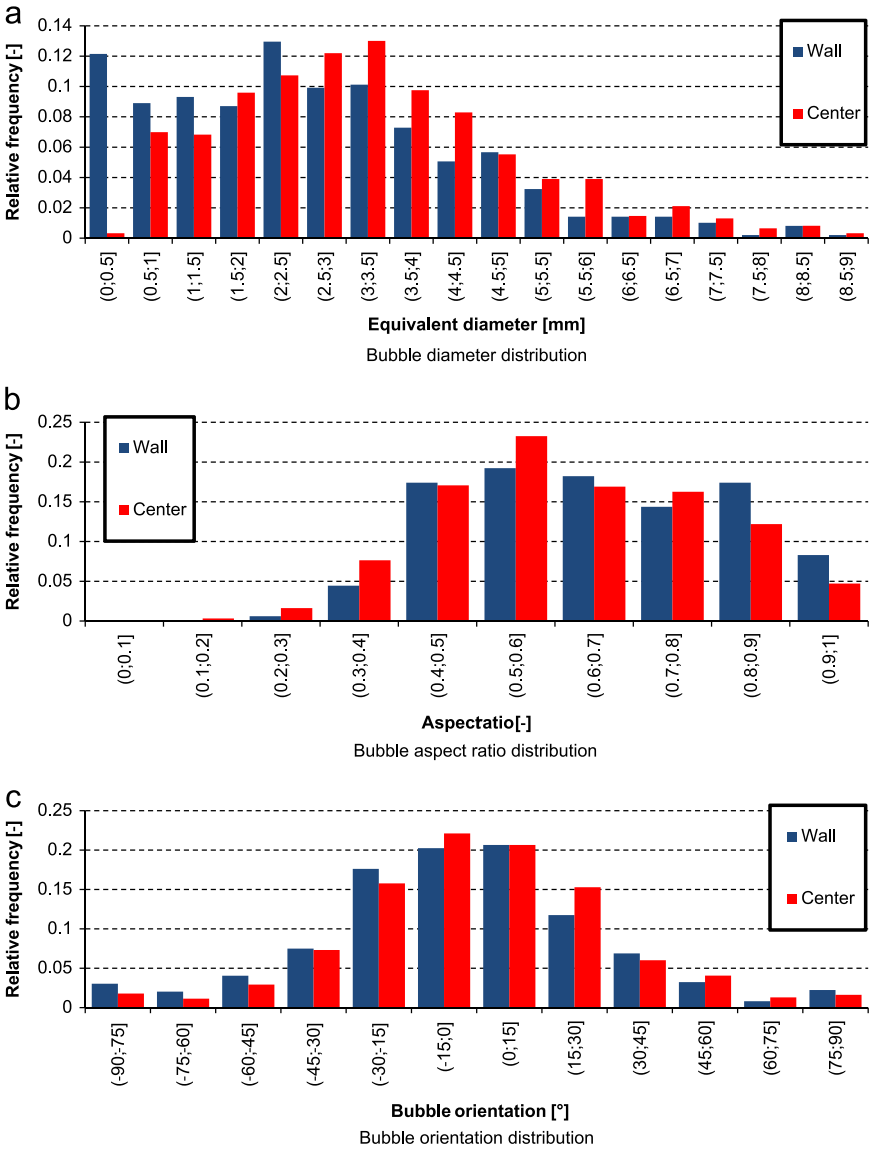

Fig. 19. Image analysis for the batch mode (U_L=0 m/s): comparison between wall and center at U_G=0.0037 m/s.

d_{eq}=3.5 mm (U_G=0.0037 m/s) and d_{eq}=4 mm (U_G=0.0074 m/s). Except for the frequency peak at low d_{eq}, the BSDs near the wall and at the center of the column are similar. Therefore, the bubbles sampled at the wall may represent the bubble shapes and size distributions in the column, which agrees with the findings of Besagni and Inzoli (2016b). Fig. 21a displays the BSDs (sampled at the wall) for the different superficial gas velocities. Up to U_G=0.0149 m/s, the BSDs are bimodal: the first peak of frequency occurs between d_{eq}=0.5 mm and 1 mm, whereas the second peak, depending on U_G, ranges between d_{eq}=2.5 mm and 3.5 mm. The presence of two maxima is also observed in the distribution of the equivalent diameters in each individual photograph. At U_G=0.0188 m/s, the BSD changes from bimodal to unimodal and is shifted toward higher bubble diameters with a peak between d_{eq}=3.5 mm and 4 mm (also, for $U_G > 0.0188$ m/s, the small bubbles were not observed). This behavior may occur because U_G=0.0188 m/s is close to the regime transition. This result agrees with the studies concerning the size of the bubbles and the flow regime transition (Lucas et al., 2003) and the findings of Besagni and Inzoli, (2016b) for an annular gap bubble column. In the literature, a bimodal distribution was found by different authors (Hernandez-Aguilar et al., 2004; Lau et al., 2013b; Parthasarathy and Ahmed, 1994; Wongsuchoto et al., 2003). Lau et al. (2013b) and Wongsuchoto et al. (2003) observed a transition from a unimodal distribution to a bimodal distribution with increasing U_G. This change in the distribution of bubble size has been justified with increased coalescence (Lau et al., 2013b) or break-up (Wongsuchoto et al., 2003). This may appear to contradict with our results; however, the present configuration (large-diameter bubble column with spider sparger) is different from the cases reported in the literature. Photographs are unavailable at a lower gas flowrate, and it is therefore impossible to verify a possible first passage from unimodal distribution to bimodal distribution. However, our BSDs are obtained by sampling the bubbles near the wall, and the equivalent BSD at the center of the column may be unimodal, as previously discussed. It is worth noting the poly-dispersed nature of the bubble size distributions with respect to the change in lift force direction at a bubble diameter of 5.8 mm (for the air–water system at ambient conditions). The poly-dispersed homogeneous regime is probably a consequence of the sparger with large openings. The BSDs discussed above were obtained at h=2.4 m from the sparger and are assumed to be representative of the developed flow. This is verified in Fig. 23, in which the BSDs (U_G=0.0111 m/s) at h=2.4 m and the BSD at

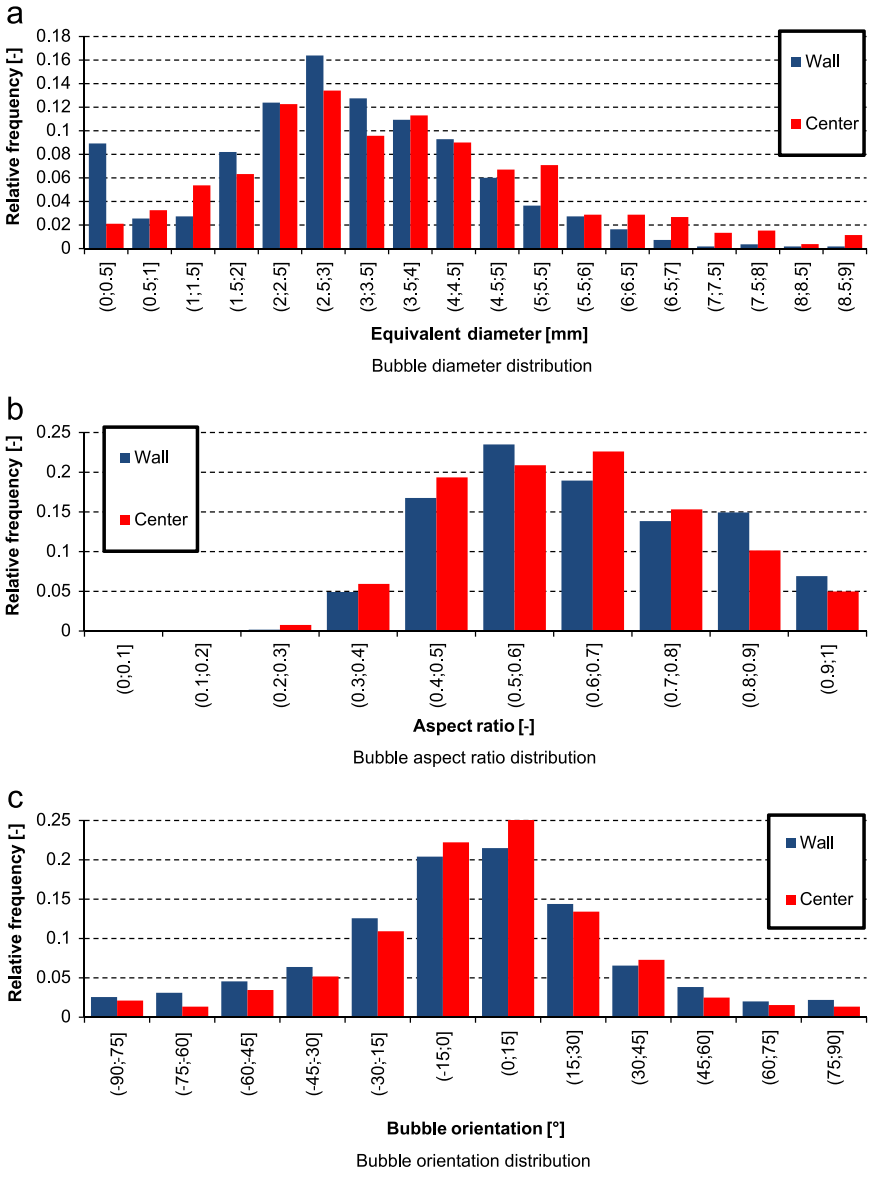

Fig. 20. Image analysis for the batch mode (U_L=0 m/s): comparison between wall and center at U_G=0.0074 m/s.

h=1.4 m are compared: the BSDs are similar, confirming that the flow is developed. This agrees with the literature: according to Thorat et al. (1998), at $h/d_c > 5$, the holdup profile is fully developed (then, the BSD is approximately constant) and, in this case, the images taken at h=1.4 m correspond to h/d_c=5.83.

The main difference in the counter-current mode (Fig. 24a), compared with the batch mode BSDs, is that the distributions are mostly unimodal with a peak between 3.5 mm and 4.5 mm (except for U_G=0.0111 m/s, with a BSD slightly shifted toward the lower diameters and a peak at approximately 3 mm). The change from bimodal to unimodal distribution and the shift toward higher diameters may be due to the lift force pushing the small bubbles toward the center of the pipe. Indeed, in the counter-current mode, "*small bubbles*" (having a positive lift coefficient) migrate toward the center of the column (please, refer to the discussion concerning the lift force in the first paragraph of this section). This is confirmed by the DNS studies of Lu et al. (2006) and Lu and Tryggvason (2007, 2013). A shifted of the BSD toward the higher diameters, in the counter-current mode (U_L= −0.04 m/s), was also observed by Besagni and Inzoli (2016b) in annular gap bubble column. We may also compare our results with the findings of Sundaresan and Varma (1990). Their results confirm the change in BSD from a wide distribution, at low flowrates, to a narrower BSD, at higher flowrates. However, their BSDs are shifted to lower values probably because of the different experimental setups and operating conditions: different sparger, smaller bubble column (d_c=0.0093 m, h_c=1 m high, lower aspect ratio), and different U_L.

3.3.1.2. Bubble shapes. Figs. 19b and 20b display the aspect ratio, ϕ, distributions at the wall and at the center of the column for U_G=0.0037 m/s and U_G=0.0074 m/s, respectively. At the center of the column, the two aspect ratio distributions are similar: approximately 5% of the bubbles can be approximated as a sphere, with φ between 0.9 and 1; 86–88% of the bubbles have $0.4 \leq \varphi \leq 0.9$, with a peak between 0.5 and 0.6; and the remaining 7–10 % are very stretched on the major axis, with $0.3 \leq \varphi \leq 0.4$. At U_G=0.0037 m/s, near the wall, the number of spherical bubbles increases, and the distribution of the aspect ratio moves toward a higher aspect ratio. At U_G=0.00074 m/s, the number of bubbles with an aspect ratio between 0.5 and 0.7 increases. Fig. 21b displays the aspect ratio distribution for the different U_G values (near the wall). The aspect ratio distributions for U_G=0.0111 m/s and

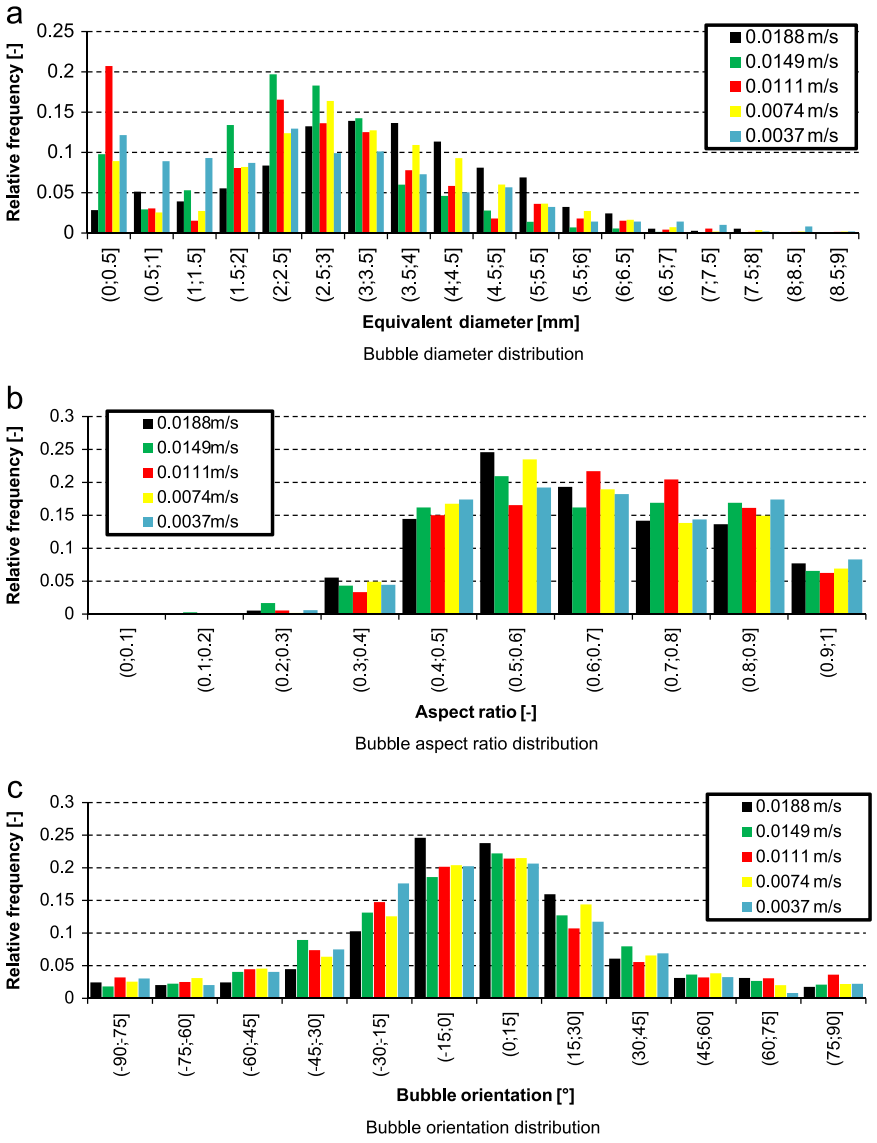

Fig. 21. Image analysis for the batch mode (U_L=0 m/s): influence of U_G (wall samplings).

U_G=0.0147 m/s are similar to U_G=0.0074 m/s: approximately 6–7% of the bubbles have φ between 0.9 and 1, 87–90% of the bubbles have $0.4 \leq \varphi \leq 0.9$, and 4–6% have $0.3 \leq \varphi \leq 0.4$. At U_G=0.0188 m/s, there is a change in the distribution, and more significantly distorted bubbles appear. This agrees with the change in the bubble size distribution and is caused by the onset of the flow regime transition, in which larger bubbles appear (gas disengagement measurements, Section 3.1.1). Fig. 22 displays the relationship between the aspect ratio and the equivalent diameter (the φ–d_{eq} space). As expected, a relation between the size and the aspect ratio of the bubbles seems to exist: the small bubbles have a high aspect ratio, whereas the larger bubbles seem to be characterized by lower aspect ratios. Indeed, bubbles with equivalent diameters less than 1 mm have an aspect ratio greater than 0.7. This means that the small bubbles tend to be spherical. Bubbles with higher equivalent diameters are characterized by lower aspect ratios (between 0.4 and 0.7), which reveals the trend of larger bubbles to be flatter. At U_G=0.0037 m/s and U_G=0.0074 m/s, the aspect distribution is compared near the wall and at the center of the column (Fig. 22a, b and Fig. 22c, d, respectively). Near the wall, there is a slightly higher number of small bubbles ($\phi > 0.7$, $d_{eq} < 2$); however, despite this small difference, the data cover almost the same φ–d_{eq} space. This suggests that the shape of the bubbles is not influenced by their position in the column, as expected. All operating conditions—until U_G=0.0147 m/s—have a comparable φ–d_{eq} distribution (Fig. 22a, c, e and f); at U_G=0.0188 m/s (Fig. 22g), there is a change in the distribution with the appearance of larger and more distorted bubbles. It is worth noting that—owing to the point selection for ellipse fitting—the smaller the bubble, the larger the error of estimation. In principal, this should change the results in Fig. 22, thus causing the low diameter data to have a higher aspect ratio. No general relation seems to exist between the aspect ratio and the position of the bubbles for the considered cases, so these data are not presented here. These results agree with the analysis of Besagni and Inzoli (2016b) concerning the aspect ratio distributions in an annular gap bubble column.

In the counter-current mode (Figs. 24b and 25), there is a lower number of spherical bubbles and a larger number of distorted/ellipsoidal bubbles: this may be caused by the higher shear stress between the phases. Indeed, the BSDs were shifted toward higher diameters. There is not a remarkable difference between the different U_G values (Fig. 24b), except for U_G=0.0037 m/s (with a larger number of bubbles with a lower aspect ratio). At U_G=0.0037 m/s, approximately 3% of the bubbles have φ between 0.9 and 1, 83% of the bubbles have $0.4 \leq \varphi \leq 0.9$, and 13% have

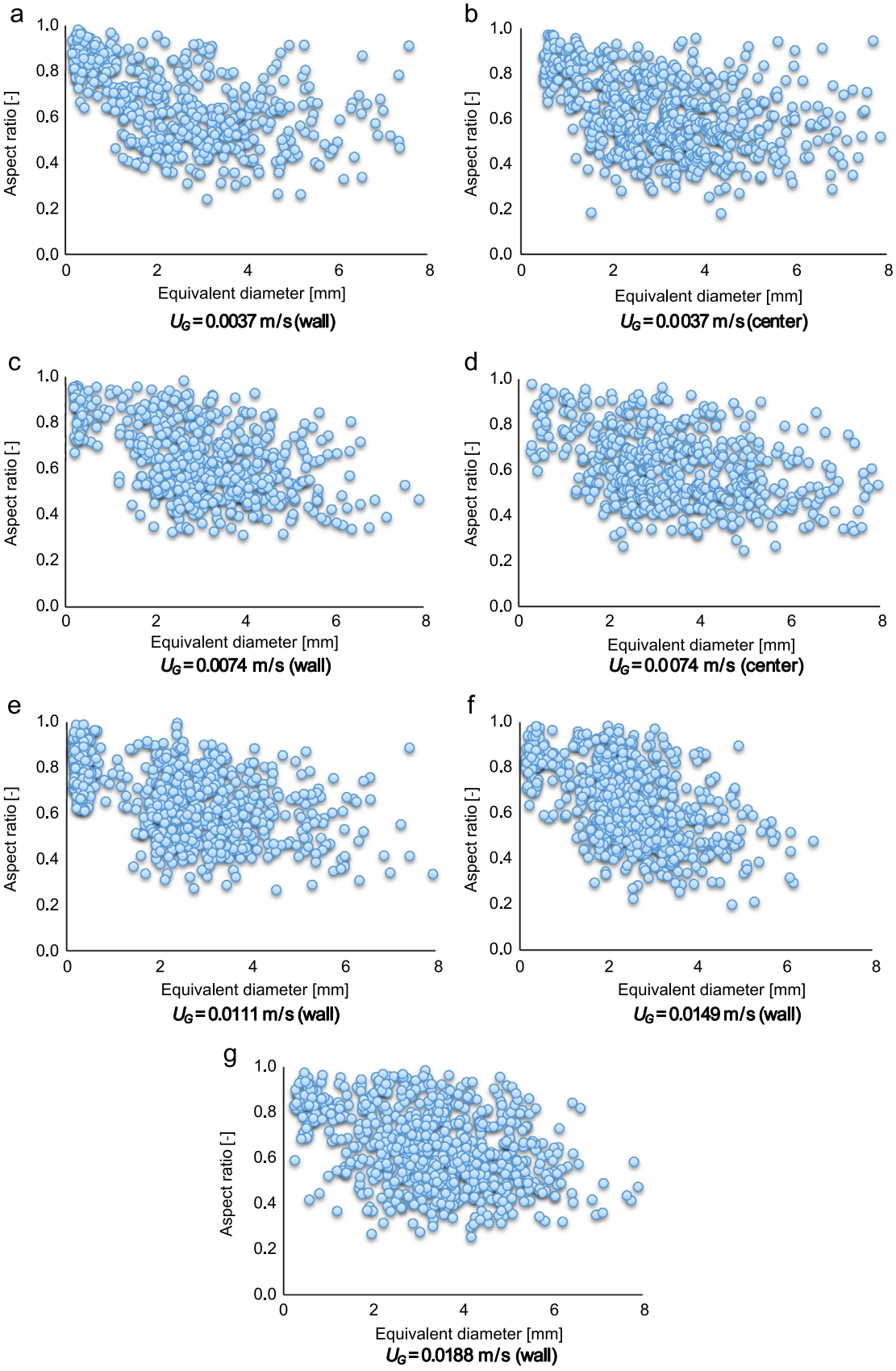

Fig. 22. Image analysis for the batch mode (U_L=0 m/s): relationship between the aspect ratio and the equivalent diameter.

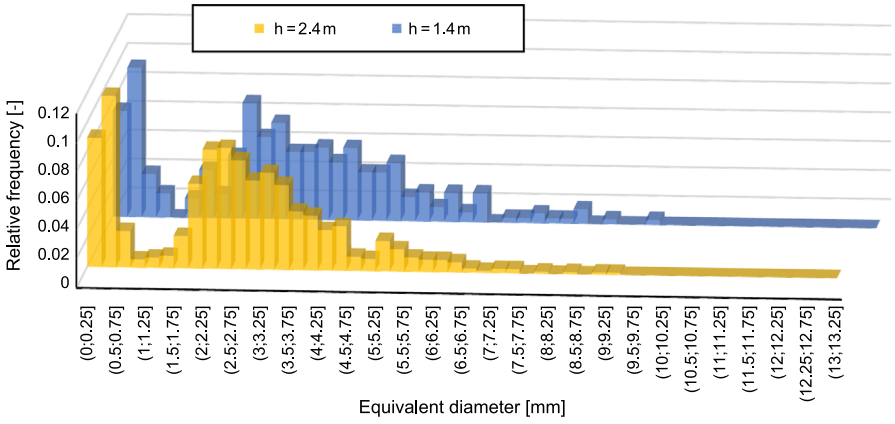

Fig. 23. Comparison of BSDs sampled at $h=2.4$ m and $h=1.4$ m from the sparger ($U_G=0.111$ m/s).

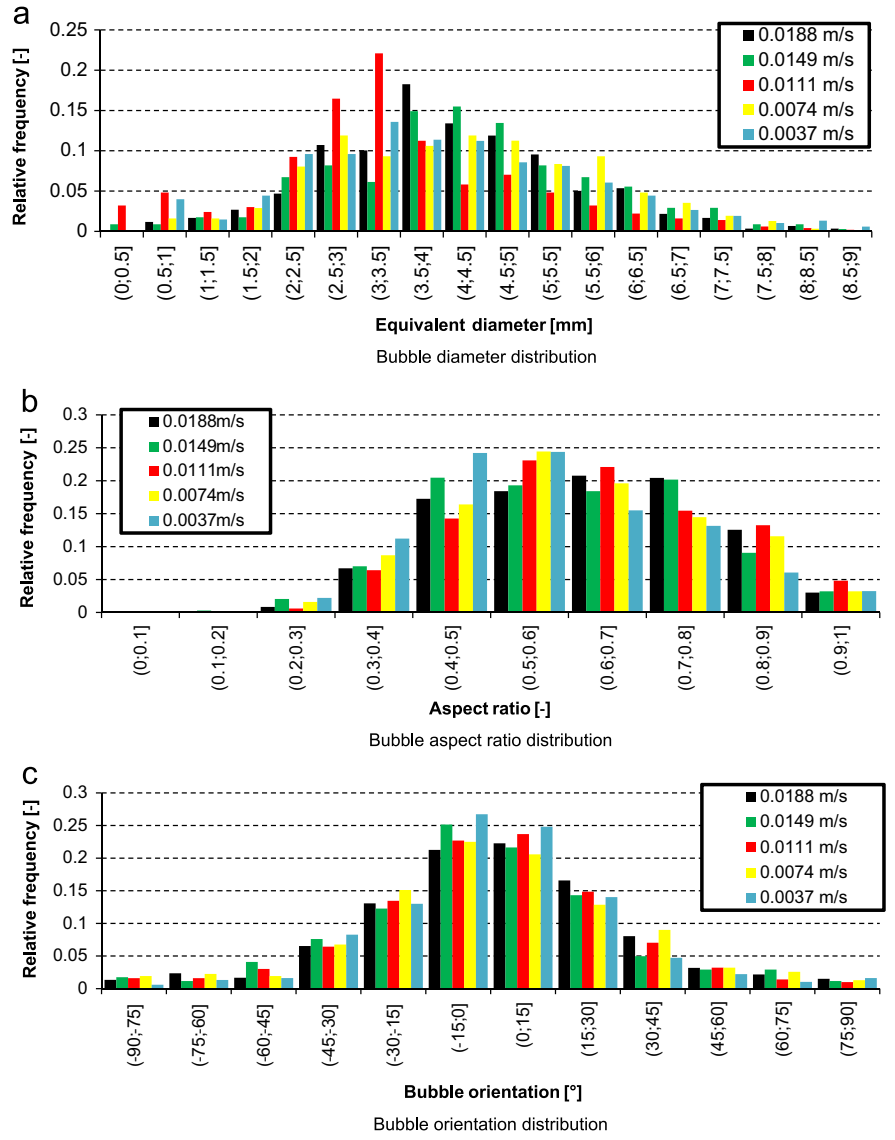

Fig. 24. Image analysis for the counter-current mode ($U_L=-0.066$ m/s): influence of U_G (wall samplings).

$0.3 \leq \varphi \leq 0.4$. For the other cases: approximately 3–5% of the bubbles can be approximated as a sphere, with φ between 0.9 and 1; 89–86% of the bubbles have $0.4 \leq \varphi \leq 0.9$, with a peak between 0.5 and 0.6; and the remaining 7–10% are very stretched on the major axis, with $0.3 \leq \varphi \leq 0.4$. All operating conditions have a comparable φ–d_{eq} space (Fig. 25), and—as previously noted—the small bubbles have a high aspect ratio, whereas the larger bubbles seem to be characterized by lower aspect ratios.

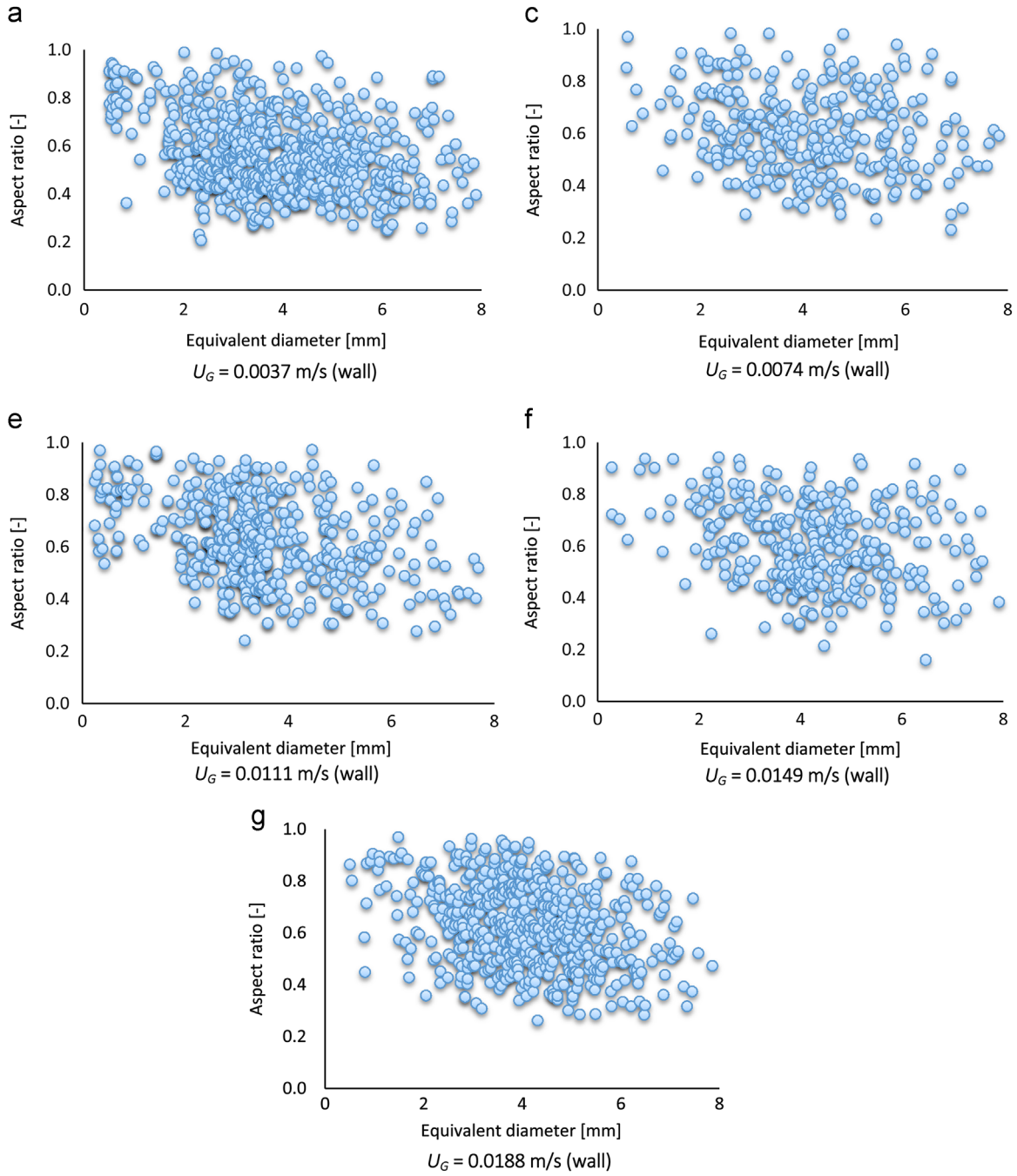

Fig. 25. Image analysis for the counter-current mode ($U_L = -0.066$ m/s): relationship between the aspect ratio and the equivalent diameter.

3.3.1.3. Bubble orientation. Figs. 19c, 20c and 21c display the distributions of bubble orientation in the batch mode for the operating conditions discussed above. Comparing the bubble orientation distributions, they are similar in shape. The only remarkable difference is at U_G=0.0188 m/s, where there are more bubbles with a lower angle of orientation. Generally, 50% of the bubbles have an orientation between −15° and +15°. Seventy-five percent of the bubbles have an orientation between −30° and +30°. In the counter-current mode (Fig. 24c), there is a larger number of bubbles with a lower angle of orientation: 60% of the bubbles have an orientation between −15° and +15°. Eighty percent of the bubbles have an orientation between −30° and +30°. These distributions may indicate that the bubbles move predominantly upward with a zigzag motion at angles ranging from −30° to 30°.

3.3.1.4. Bubble Sauter mean diameter. Fig. 26 compares the Sauter men diameter for the batch and counter-current mode (wall-samplings). The Sauter mean bubble diameter is computed as:

$$d_{23} = \frac{\Sigma_i^N n_i d_{Bi}^3}{\Sigma_i^N n_i d_{Bi}^2} \tag{37}$$

where d_{Bi} and n_i are the diameter and number of bubbles of size class i, respectively, and N is the number of classes used for the distribution. In the counter-current mode, for the same gas velocity, the mean diameter decreases. This may be related to the enhanced breakup owing to the higher turbulence in the pipe.

3.3.1.5. Comparison with the literature. For bubbles rising in an infinite medium, Clift et al. (1978) proposed a graphical correlation to determine the shapes of the bubbles in terms of *Eo*, *M* and *Re*. *M*

is defined only by the properties of the fluids; for a constant M, the shapes of the bubbles evolve from spherical to ellipsoidal to cap-shaped with increasing equivalent diameter. Clift et al. (1978) evaluated influence of the wall on the rising bubbles according to the ratio λ between the equivalent diameter of the bubble and the diameter of the system. For values of λ less than 0.6, the walls have little influence, and the rising bubble can be considered as if rising in an infinite medium. Herein we focus on the batch mode only (for the sake of clarity): the largest bubble detected in this analysis had an equivalent diameter of 12 mm, and the hydraulic diameter of the column is equal to 240 mm. The maximum value of λ is therefore 0.13. Thus, the effect of the wall can be neglected as a first approximation. The data are represented in Fig. 27. With regard to the shapes of the bubbles, the data obtained from the analysis of the images agree with the diagram by Clift et al. (1978): the bubbles sampled cover the spherical and ellipsoidal area. There is no bubble in the area of the cap-bubbles; indeed, cap-bubbles were not detected. The same procedure may be applied to the counter-current mode and results in the same conclusions. These results agree with the literature comparison of Besagni and Inzoli (2016b), for an annular gap bubble column.

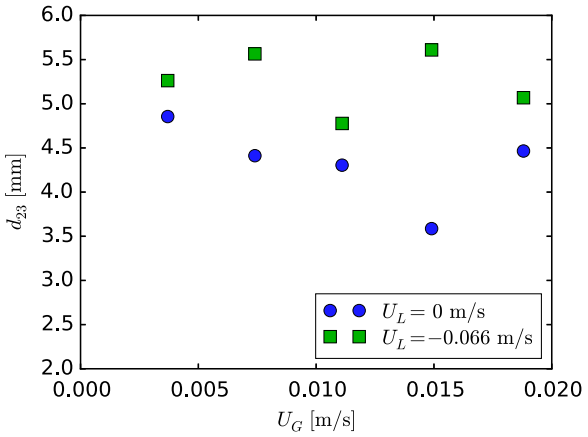

Fig. 26. Sauter mean diameter: comparison between the batch and counter-current modes.

3.3.2. Near sparger

3.3.2.1. Near sparger phenomena. It is clear from the flow visualizations (Figs. 18 and 19) that the hole activation depends on the air flowrate. This is further proof of the maldistribution regime caused by the sparger.

In the this region, we observed the same phenomena as described by Hur et al. (2013):

- *Nucleating bubbles* (Fig. 28a)**:** the bubble is forming on the surface of the orifice of the sparger.
- *Channeling* (Fig. 28b)**:** with increasing gas superficial velocity, the bubble nucleating on the orifice is affected by the wake of the preceding bubble and thus is trailed and accelerated. In this

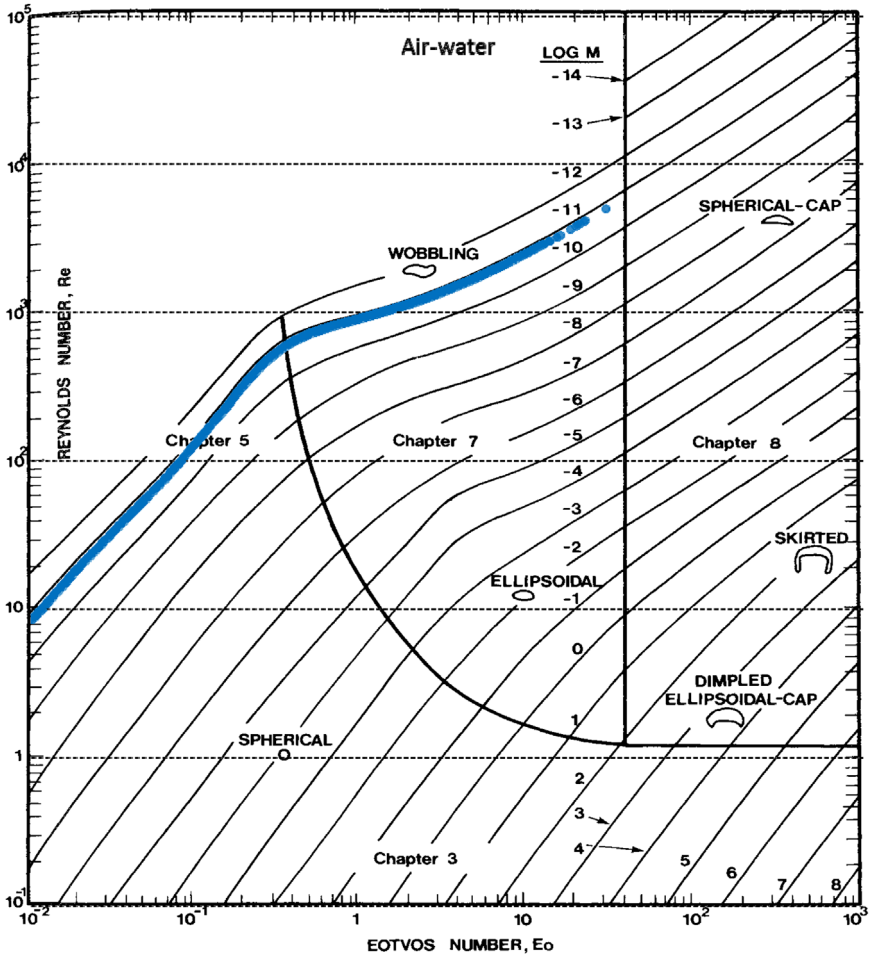

Fig. 27. Data obtained for the batch mode plotted on the Clift diagram.

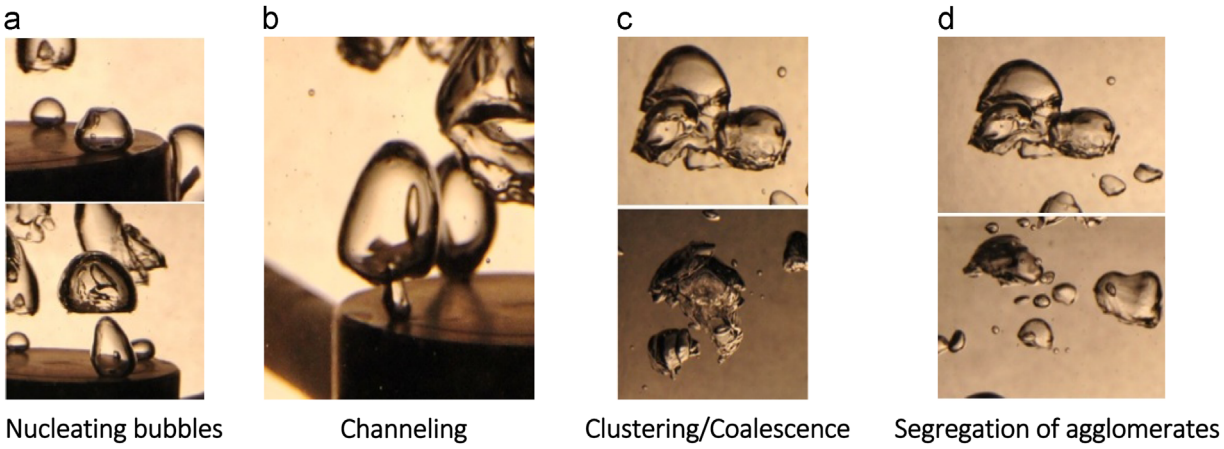

Fig. 28. Bubble shape and phenomena near the distributor.

way, the channeling effect creates bubbles with a peculiar shape that are still attached to the orifice by their bottom, thus, larger bubbles are nucleated and are encountered only on the gas sparger surface.

- *Clustering/coalescence* (Fig. 28c)**:** above the sparger orifices, agglomeration occurs owing to the bubble wakes that accelerate the trailing bubbles. This phase normally involves low energy collisions that do not lead to coalescence. Only when the colliding bubbles have sufficient energy and remain in contact for enough time can coalescence occur.
- *Segregation of agglomerates* (Fig. 28d)**:** coalescence hardly occurs within clusters of bubbles because of the low energetic collisions. Therefore, the agglomerates segregate a short time later, resulting in multiple bubbles that rise distinctly.

3.3.2.2. Bubble size distributions. At first, the bubble size distribution in the sparger region is analyzed by sampling all bubbles from the sparger up to $h \approx 0.2$ m above the sparger itself. The results are presented in Fig. 29a and b for the batch and counter-current modes, respectively. Fig. 29a displays the sparger BSDs for the different superficial gas velocities. In all conditions, the BSD covers the range from the low to high equivalent diameter (up to 22.5 mm). At $U_G = 0.0037$ m/s, the BSD is unimodal with a peak at approximately $d_{eq} = 3.5$ mm; with increasing air flowrate, at $U_G = 0.0074$ m/s, the peak moves toward a lower equivalent diameter (approximately 1 mm). With increasing U_G, the BSDs change, and an absolute maximum is always observed at approximately 1 mm, whereas multiple relative maxima are found for higher diameters. Although the large bubbles have low relative frequencies, they are strictly non-negligible owing to their large volume. At $U_G = 0.0037$ m/s and $U_G = 0.0074$ m/s, the BSDs have a large peak in the low diameter range (approximately 1 mm) and extend towards higher equivalent diameters. For the higher gas velocities, the BSDs change to bimodal: the first frequency peak is at approximately $d_{eq} = 1$ mm (but it is lower if compared with the batch mode), and the second peak is at approximately $d_{eq} = 3$ mm and 3.5 mm. Compared with the batch mode, the counter-current mode (Fig. 29b) changes the shape of the BSD from bimodal to unimodal and moves the BSD toward a larger diameter. The latter effect was also reported by Besagni and Inzoli (2016b). It is worth noting that these results consider a wide region (0.2 m above the sparger) where coalescence and break-up phenomena already occur. Therefore, additional bubble sampling (in the batch mode only) is performed by considering only the bubbles freshly detached from the sparger, which were unaffected by the coalescence and break-up phenomena. This sampling was conducted considering many images and focusing the camera near the sparger openings. The results are displayed in Fig. 30a for the different U_G values. In this region, the BSDs are shifted toward the higher diameter and cover only bubbles with $d_{eq} > 7$ mm. These bubbles are unstable and will break into smaller bubbles. Indeed, the bubbles in this region have equivalent diameters higher that the critical ones (10.1–12.8 mm) reported by Besagni and Inzoli (2016b); on the other hand, in the developed region, the bubble equivalent diameters are below these values. The bubble side distributions change because of the coalescence and break-up phenomena (Fig. 30b). It is worth noting that the BSD at the sparger depends on many design parameters (i.e., the hole of the sparger and the flowrate) as reported by Hur et al. (2013) and Geary and Rice (1991). For example, a sensitivity analysis made by Cao et al. (2009) using the Geary and Rice (1991) model showed that increasing hole flowrate or decreasing hole dimensions lead to larger bubbles, whereas an increasing number of holes results in smaller bubbles detaching from the sparger.

3.3.2.3. Comparison with the literature. The data obtained by sampling only the bubbles freshly detached from the sparger (Fig. 30a) can be compared with the correlations of Polli et al. (2002) and by Cao et al. (2009). These correlations are based on non-dimensional numbers—the "*dimensionless bubble diameter*" d_w and the "*dimensionless velocity*" N_w:

$$d_w = d_v \left(\frac{g \rho_L}{d_o \sigma} \right)^{\frac{1}{3}} \tag{38}$$

$$N_w = \frac{We}{Fr^{1/2}} \tag{39}$$

where d_v and Fr are the volumetric mean bubble diameter and the Froude number, respectively, defined as:

$$d_v = \left(\frac{\sum {d_{eq}}^3}{n_{tot}} \right)^{\frac{1}{3}} \tag{40}$$

$$Fr = \frac{{u_{th}}^2}{g d_H} \tag{41}$$

where n_{tot} is the number of bubbles sampled, and u_{th} is the gas velocity through the hole. Cao et al. (2009) and Polli et al. (2002) assumed that d_w is well estimated with the dimensionless correlation of Miyahara et al. (Miyahara and Hayashino, 1995) for values of N_w lower than 14 and 10, respectively. For higher N_w, their correlations are obtained by fitting experimental values with an exponential function, as suggested by Miyahara and Hayashino (1995). The two correlations predict the trend of the experimental data, and in particular, the Cao correlation well fits

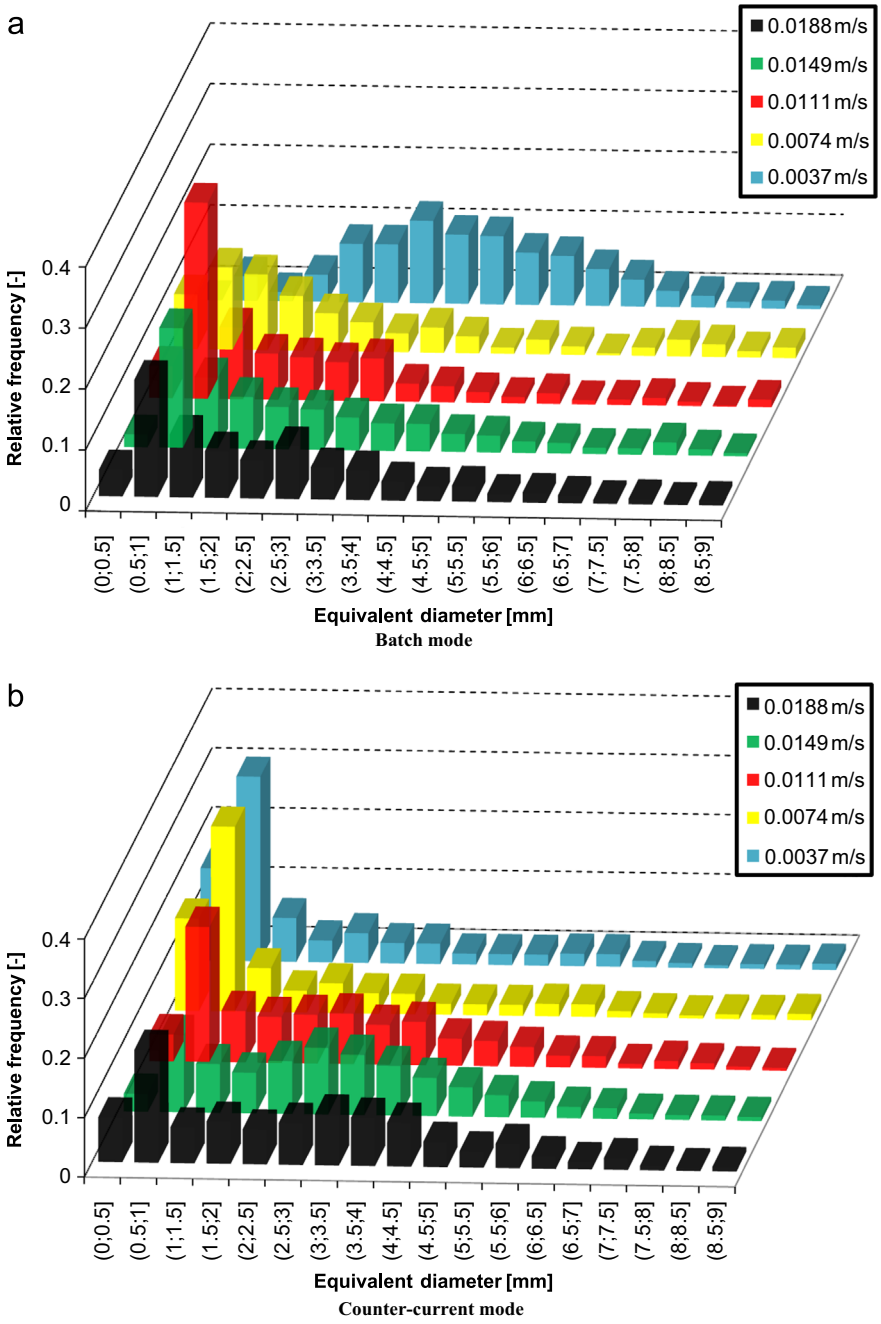

Fig. 29. Bubble size distribution at the sparger: comparison between the batch and counter-current modes.

the experimental value (Fig. 31a). Only two points do not match the correlation, probably because of differences in sparger design (the authors used a ring sparger). The aim of these correlations is to predict the BSD at the sparger using the design parameters as the inputs: by knowing all quantities concerning N_w, through the correlation, it is possible to obtain d_w and, finally, d_v. Under the hypothesis that the BSD is lognormal, the predicted BSD is expressed by:

$$f(d_{eq}) = \frac{1}{\sqrt{2\pi}d_{eq}} exp\left[-\frac{1}{2}\left(\frac{\ln d_{eq} - m}{\sigma_D}\right)\right] \quad (42)$$

Where m is the logarithm of d_v. By applying the Cao et al. (2009) correlation for obtaining d_v and using $\sigma_D = 0.19$ as the standard deviation—in accordance with Cao et al. (2009)—the predicted and experimental BSDs are in good agreement (Fig. 30b).

3.4. Optical probe

The optical probe measurements consist of radial profiles at two different axial positions: in the developed region ($h = 1.9$ m from the sparger) and closer to the sparger ($h = 0.7$ m from the sparger)

3.4.1. Developed region

Figs. 32 and 33 display the radial profiles of the local void fractions and bubble rise velocities: Fig. 32 focuses on the batch mode, whereas Fig. 33 displays the influence of the counter-current mode ($U_L = -0.066$ m/s). Fig. 34 displays the radial profiles of the Sauter mean diameters in batch (Fig. 34a) and counter-current (Fig. 34b) modes.

The local void fraction profiles are center peaked, which may appear to be surprisingly: in the homogeneous regime, the void

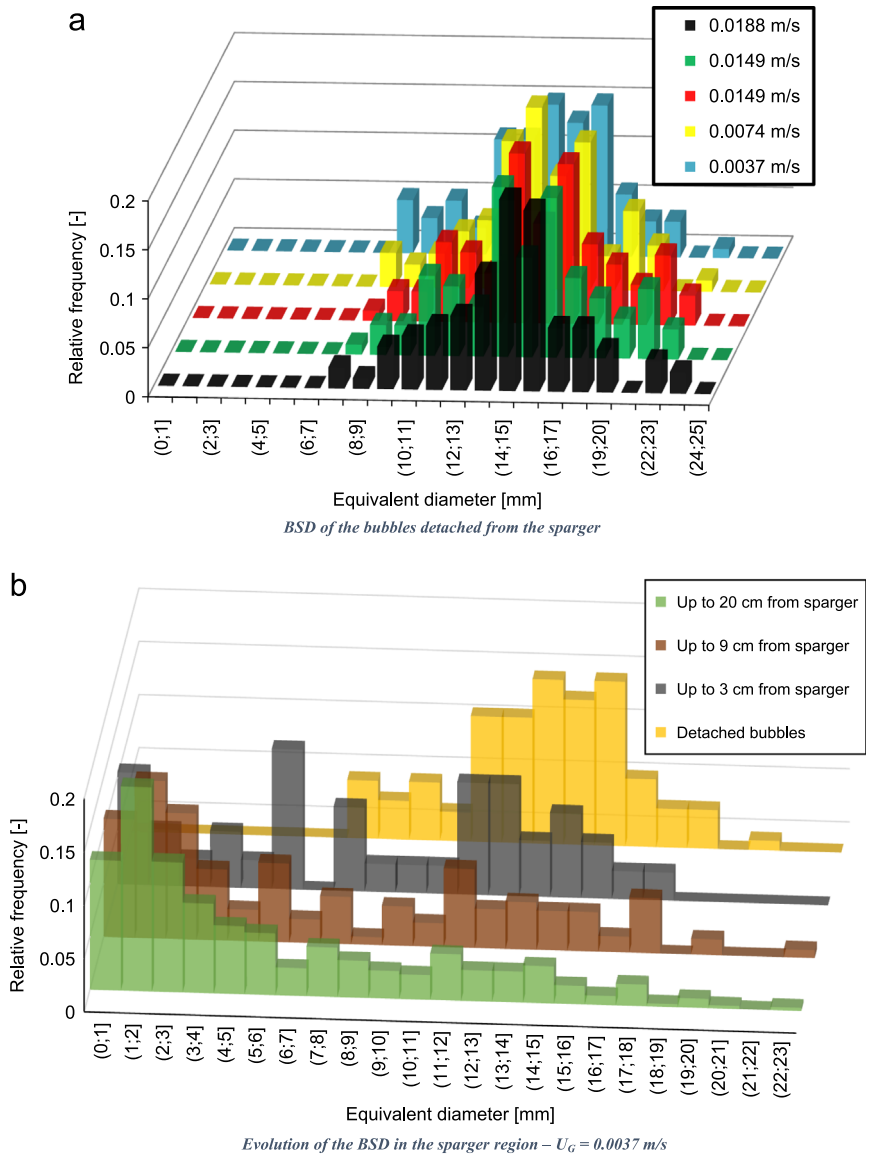

Fig. 30. Bubble size distribution at the sparger: near sparger sampling and flow development.

fraction profiles are usually somewhat flat. This behavior may be caused by the spider sparger with the large openings, which produces a poly-dispersed flow in the column (Section 3.3). In this respect, the center peaked profiles in the homogenous regime may be induced by the bubbles with an equivalent diameter larger than 5.8 mm, thus having a lift force pushing them towards the center of the pipe. The center peaked profiles in the homogeneous regime suggest the existence of a maldistribution regime. Increased gas flowrates resulted in overall higher void fractions and greater profile curvature from the column wall to the center, particularly after the flow regime transition. Indeed, after the transition point, the formation of "*coalescence-induced*" bubbles (Section 3.1.1) led to increased curvature of the radial profiles, where maximum local holdups occurred at the center of the column. The existence of a pronounced radial holdup profile, which generates strong liquid recirculation, is a characteristic of the heterogeneous regime. The local void fractions were compared to global holdups by integrating the radial measurements over the column cross-sectional area:

$$< \varepsilon_G > = \frac{1}{\pi R_C^2} \int_0^{R_C} \varepsilon_{G,Local} 2\pi r dr \tag{43}$$

where R_C is the radius of the column. Table 5 shows that the relative errors between the integrated local measurements ($< \varepsilon_G >$) and the global holdups (ε_G), with the exception of low U_G, are below 20%. This agrees with the study of Pjontek et al. (2014) and Barrau et al. (1999), which reported the worst performance of the optical probes at low gas fractions. The error may also be derived from the pressure gradient along the column, which causes an axial profile in the local void fraction.

An increase in U_G leads to an increase in bubble vertical velocity, u_b, as expected (Fig. 32b). However, the increase in velocity is limited to the homogeneous regime, with the exception of U_G=0.0188 m/s, which is closer to the transition point. Above the flow regime transition, the bubble rise velocity increases because of the bubble coalescence (proved by the presence of the "*coalescence-induced*" bubbles). The increase in the bubble rise velocity reduces the gas residence time in the column, thus decreasing the holdup versus gas velocity slope (Fig. 5) and increasing the center peaked void fraction profiles (Fig. 32a). Fig. 33 displays the effect of the counter-current mode: the local void fraction is increased (Fig. 33a) by the effect of the liquid flow slowing down the rise of the bubbles (Fig. 33b). These results

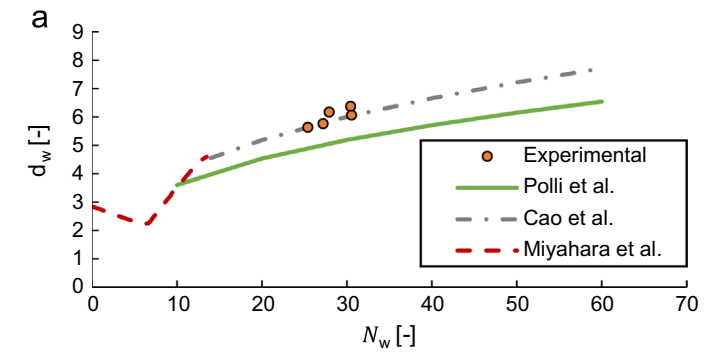

Comparison between literature correlations and experimental data

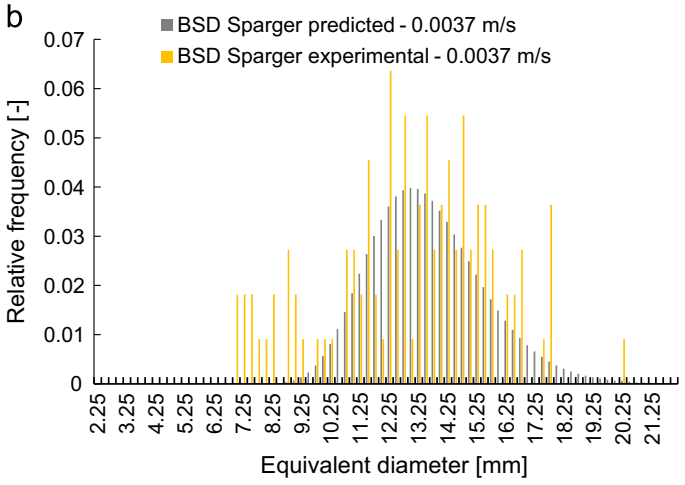

Comparison between experimental and predicted BSD at the sparger – 0.00337 m/s

Fig. 31. Near sparger sampling: comparison with the literature.

explain the behavior of the holdup curve in the counter-current mode in the homogeneous regime.

Fig. 34 displays the radial profiles of the bubble diameters as a function of U_G (Fig. 34a) and U_L (Fig. 34b) in the homogenous regime. These data were obtained by correcting the optical probe measurements (Eq. (13)) by using Eq. (14). The values of the mean aspect ratio in Eq. (14) were provided by the image analysis. Considering Fig. 34a, the bubble diameter profiles are almost constant in the cross section of the pipe. There are no remarkable differences in the bubble diameter profiles at U_G=0.0037 and U_G=0.0074 m/s; the bubble diameter profiles then increase at U_G=0.0111 and U_G=0.0149 m/s, and finally, the profile at U_G=0.188 m/s decreases (because of the lower aspect ratio due to the higher distorted bubbles near the regime transition). Considering the counter-current mode (Fig. 34b), the mean diameter decreases, probably because of the lower aspect ratio and the enhanced breakup (owing to the higher turbulence in the pipe). However, no quantitative data are available to support the second statement, and this will be a matter for future studies. The optical probe also provides bubble chord distributions: these data will be used in future studies regarding algorithms for the conversion of bubble chord distributions into bubble diameter distributions.

It is worth noting that similar results (i.e., the center peaked void fraction profiles and the influence of the counter-current mode) were obtained by Besagni and Inzoli (2016a) in the "OT" bubble column.

3.4.2. Near sparger

Figs. 35–37 display the void fraction, bubble rise velocity and Sauter mean diameter profiles at h=0.7 m from the sparger. The local void fraction profiles (Fig. 35) are more center peaked than those in the developed region. This suggests that, in this region, there is higher liquid recirculation and a larger number of large bubbles that will break into smaller bubbles. Indeed, in the sparger region, the BSDs cover larger bubble diameters compared with the developed region (Section 3.3). It is particularly interesting that at low U_G, the void fraction profile is highly asymmetric and center peaked, confirming the maldistribution regime. Thus, the sparger used (with large openings) has a non-negligible influence on the column hydrodynamics. As in the developed region, increased gas flowrates resulted in overall higher void fractions and greater profile curvature from the column wall to the center, particularly after the flow regime transition. As expected, the presence of larger bubbles at higher U_G leads to increased curvature of the radial profiles. Concerning the bubble vertical velocity (Fig. 36), u_b, an increase in air superficial velocity leads to an increase in bubble vertical velocity, as expected. However, the increase in velocity is limited to the homogeneous regime. It is worth noting that, contrary to the developed region, also at U_G=0.0188 m/s, the bubble rise velocity profile is similar to that for lower U_G. This result suggests that the "*coalescence-induced*" bubbles—which cause the regime transition—begin to appear at approximately this gas velocity, probably above this measurement section. This will be a matter for future studies. Finally, Fig. 37 displays the radial bubble diameter profiles (corrected by Eq. (14)) as a function of U_G: the Sauter mean diameter is larger compared with the developed region, as expected and previously discussed.

4. Conclusions

We have experimentally studied a counter-current bubble column (0.24 m inner diameter and 5.3 m height), considering gas superficial

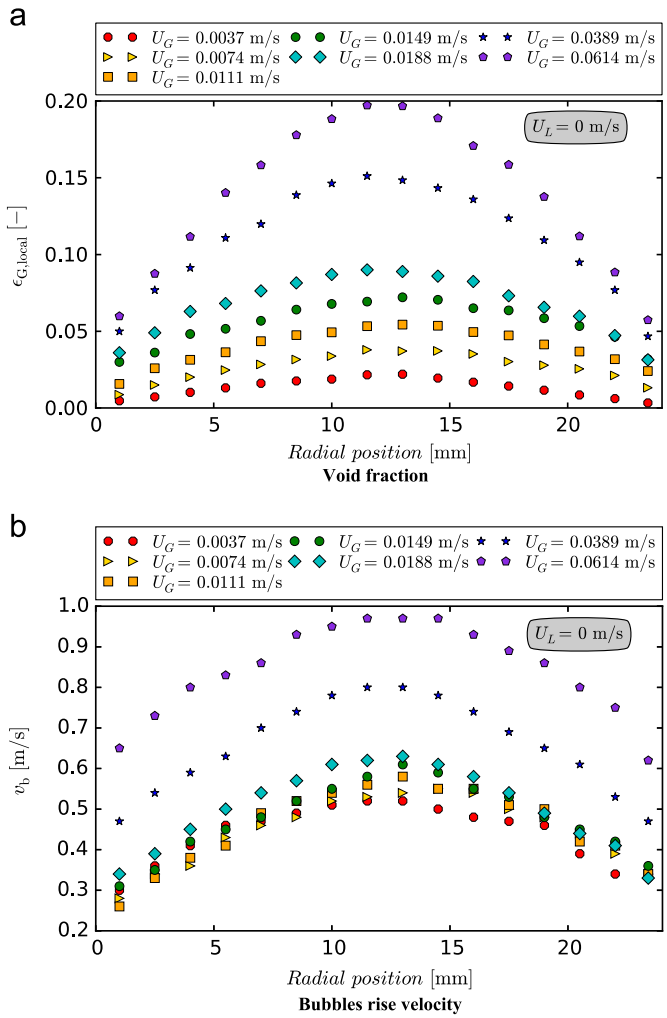

Fig. 32. Optical probe data (h=1.9 m from the sparger): void fraction and bubble rise velocity profiles – batch mode (U_L=0 m/s).

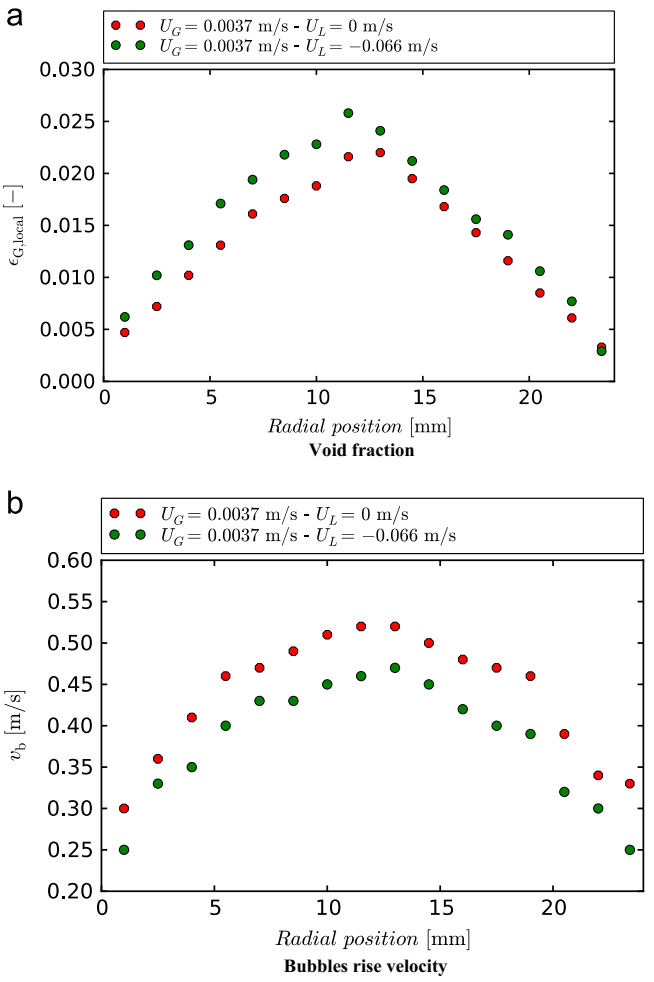

Fig. 33. Optical probe data (h=1.9 m from the sparger): void fraction and bubble rise velocity profiles – counter-current mode (U_L= −0.066 m/s).

velocities in the range of 0.004–0.20 m/s and liquid superficial velocities up to −0.09 m/s. A variety of techniques is applied to study the influence of the counter-current mode on holdup, flow regime transition, bubble size distribution and local flow properties.

The main results are as follows:

- Two regimes (the homogeneous and transition regimes) have been identified, and the transition points between them have been evaluated. In the homogeneous regime, the holdup increases linearly as a function of U_G, and it increases with U_L. In the transition regime, the influence of the superficial water velocity on the holdup decreases. The counter-current mode destabilizes the homogeneous regime: the transition point lies in the range between 0.0264 m/s and 0.0173 m/s depending on the liquid velocity. Above the regime transition, "*coalescence-induced*" bubbles, rising in the column at higher velocities, appear.
- The holdup data have been compared with data taken from the literature and with a set of correlations. Comparing the holdup data obtained with our previous studies, we observe a limited influence of the sparger design in large-diameter bubble column, possibly due to the sparger with large opening. In addition, a new correlation for the holdup was proposed.
- In the batch mode, the BSDs are poly-dispersed and bimodal; the small bubbles are more concentrated near the wall, probably because of the lift force. We observed a change in the bubble size distribution (from bimodal to unimodal) near the flow regime transition. In the counter-current mode, larger bubbles are pushed toward the wall—probably owing to the lift force—and the bubble size distribution are shifted toward larger diameters. The relations between the bubble size and shape have been discussed. In particular, the counter-current mode produces a change in the bubble shape distribution (i.e., more distorted bubbles appear).
- Near the sparger, the bubble size distributions are shifted toward higher diameters; however, these large bubbles are unstable and break into smaller ones. The results agree with correlations found in the literature.
- The local flow properties are a function of both the axial and radial positions in the bubble column. In the developed region of the column, the local void fraction profiles are center peaked, and increased gas flowrates result in overall higher void fractions and greater profile curvature from the column wall to the center, particularly after the flow regime transition. The void fraction profiles are center peaked even in the homogeneous regime: the spider sparger with large openings, which produces a poly-dispersed flow in the column, may cause this behavior. An increase in air superficial velocity also increases the bubble vertical velocity; however, the increase in velocity is limited to the homogeneous regime and is higher in the transition flow regime. The counter-current mode increases the local void fraction by slowing down the rise of the bubbles.
- The void fraction profiles, near the sparger, are more center peaked than those in the developed region; this suggests that in

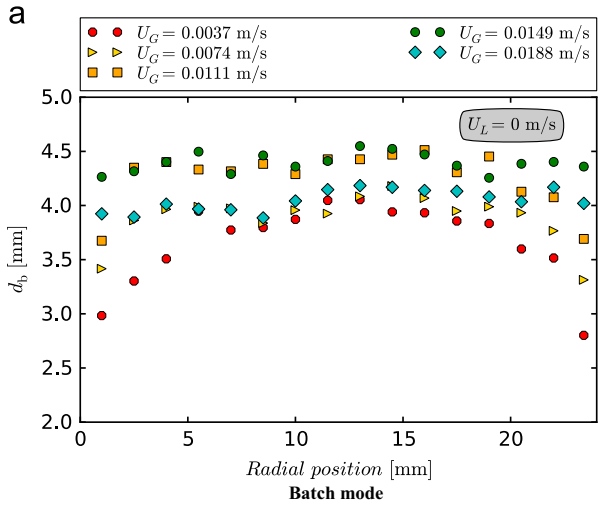

Fig. 34. Optical probe data (h=1.9 m from the sparger): bubble mean diameter.

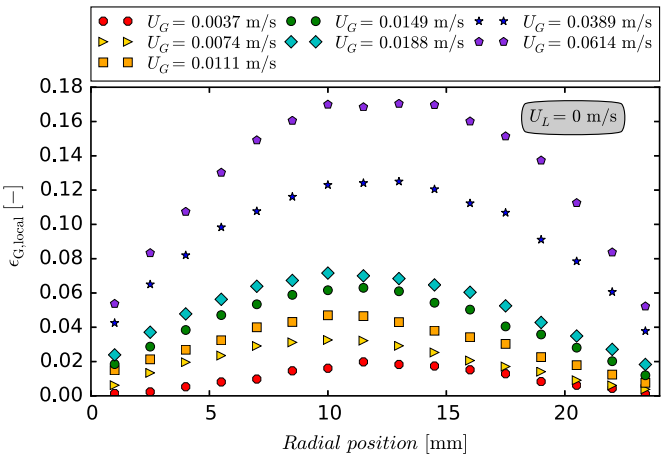

Fig. 35. Optical probe data (h=0.7 m from the sparger): void fraction profiles.

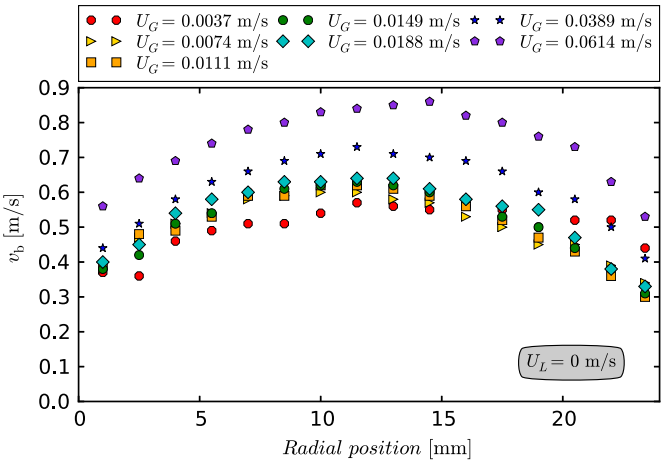

Fig. 36. Optical probe data (h=0.7 m from the sparger): bubble rise velocity.

Table 5
Comparison between local and global holdup values.

U_G [m/s]	$< \varepsilon_G >$ [%]	ε_G **[%]**	Relative error[a] [%]
0.0037	1.65	1.02	−61.06
0.0074	2.98	2.28	−30.65
0.0111	4.37	3.72	−17.47
0.0149	5.88	5.30	−10.92
0.0188	7.80	6.60	−18.13
0.0389	12.74	11.22	−13.57
0.0614	16.35	14.36	−13.89

[a] Computed using: $100 \cdot \frac{\varepsilon_G - < \varepsilon_G >}{\varepsilon_G}$.

this region, there is a larger number of large bubbles that will break into smaller bubbles as the flow develops.

In conclusion, the proposed investigation offers a comprehensive view of counter-current bubble columns and provides a large dataset with which to set up and validate numerical models.

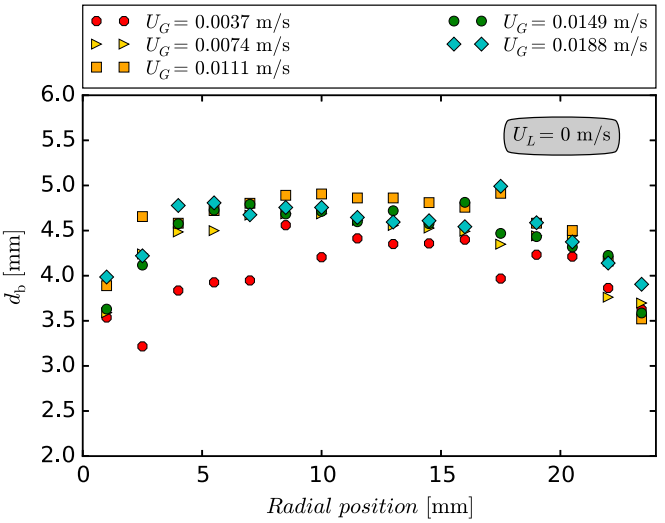

Fig. 37. Optical probe data (h=0.7 m from the sparger): bubble Sauter mean diameter.

Nomenclature

Non-dimensional numbers

$Ca = \frac{U_G \mu_L}{\sigma}$ Capillary number [dimensionless]

$d_w = d_v \left(\frac{g\rho_L}{d_o \sigma}\right)^{1/3}$ Non-dimensional diameter [dimensionless]

$Eo = \frac{g(\rho_L - \rho_G) d_{eq}^2}{\sigma}$ Eötvös number [dimensionless]

$Fr = \frac{v^2}{g d_{eq}}$ Froude number [dimensionless]

$Mo = \frac{g(\rho_L - \rho_G)\mu_L^4}{\rho_L^2 \sigma^3}$ Morton number [dimensionless]

$N_w = \frac{We}{Fr^{0.5}}$ Non-dimensional velocity [dimensionless]

$Re = \frac{\rho_L u_b d_{eq}}{\mu_L}$ Reynolds number [dimensionless]

$We = \frac{d_{eq} u_b^2 \rho_L}{\sigma}$ Weber number [dimensionless]

Acronyms

AG	Annular Gap bubble column as discussed in Besagni and Inzoli (Besagni and Inzoli, 2016a)
BSD	Bubble Size Distribution
CFD	Computational Fluid Dynamics
CI	Coalescence-induced bubbles
DNS	Direct Numerical Simulation
GD	Gas Disengagement
NCI	Non-coalescence-induced bubbles
OT	Open Tube bubble column as discussed in Besagni and Inzoli (Besagni and Inzoli, 2016a)

Symbols

a	Major axis of the bubble [m]
b	Minor axis of the bubble [m]
c	Coefficient in the ellipse equation [dimensionless]
α	Coefficient in the aspect ratio correlation [dimensionless]
A^*, B^*	Parameter in the Reilly correlation for the flow regime transition [dimensionless]
d_o	Gas sparger holes diameter [mm]
d_c	Diameter of the column [m]
d_{eq}	Bubble equivalent diameter [mm]
d_b	Sauter mean diameter from the optical probe [mm]
$d_{b,Corrected}$	Sauter mean diameter from the optical probe corrected by the bubble aspect ratio [mm]
d_{23}	Sauter mean diameter from the image analysis [mm]
d_v	Volumetric mean bubble diameter [mm]
D_H^*	Non-dimensional diameter [dimensionless]
$D_{H,Cr}^*$	Critical Non-dimensional diameter [dimensionless]
f	Bubble frequency [1/s]
n, k_1^*, k_1, k_2, k_3	Parameters in the holdup correlation [dimensionless]
H	Height from the bottom of the column [m]
H_c	Height of the column [m]
H_D	Heights of the free-surface after aeration [m]
H_0	Heights of the free-surface before aeration [m]
J	Drift flux [m/s]
g	Gravity acceleration [m/s^2]
R_c	Radius of the column [m]
S	Parameter in the swarm velocity method [dimensionless]
x	Horizontal axis [dimensionless]
x_c	Horizontal coordinate of the bubble center [m]
y	Vertical axis [dimensionless]
y_c	Vertical coordinate of the bubble center [m]
u_b	Bubble rise velocity [m/s]
u_{th}	Gas velocity through the holes of the sparger [m/s]
u_∞	Terminal bubble velocity [m/s]
U_b	Parameter in the drift flux methods (the swarm velocity) [m/s]
U	Superficial velocity [m/s]
θ	Bubble orientation [deg]
μ	Dynamic viscosity [Pa s]
σ	Surface tension [N/m]
φ	Aspect ratio [dimensionless]
ε_G	Gas Holdup [dimensionless]
$\varepsilon_{G,Local}$	Local void fraction [dimensionless]
$<\varepsilon_G>$	Integrated gas holdup [dimensionless]
$\Delta t_{sampling}$	Optical probe sampling time [s]

Subscripts

L	Liquid phase
G	Gas phase
T, E	Subscripts in the drift flux formulation
trans	Transition point
swarm	Swarm velocity

References

Akita, K., Yoshida, F., 1973. Gas holdup and volumetric mass transfer coefficient in bubble columns. Effects of liquid properties. Ind. Eng. Chem. Process. Des. Dev. 12, 76–80.

Al-Oufi, F.M., Cumming, I.W., Rielly, C.D., 2010. Destabilisation of homogeneous bubbly flow in an annular gap bubble column. Can. J. Chem. Eng. 88, 482–490.

Al-Oufi, F.M., Rielly, C.D., Cumming, I.W., 2011. An experimental study of gas void fraction in dilute alcohol solutions in annular gap bubble columns using a four-point conductivity probe. Chem. Eng. Sci. 66, 5739–5748.

Aloufi, F.M., 2011. An investigation of gas void fraction and transition conditions for two-phase flow in an annular gap bubble column. Loughborough University.

Baawain, M.S., El-Din, M.G., Smith, D.W., 2007. Artificial neural networks modeling of ozone bubble columns: mass transfer coefficient, gas hold-up, and bubble size. Ozone: Sci. Eng. 29, 343–352.

Barrau, E., Rivière, N., Poupot, C., Cartellier, A., 1999. Single and double optical probes in air-water two-phase flows: real time signal processing and sensor performance. Int. J. Multiph. Flow 25, 229–256.

Besagni, G., Guédon, G., Inzoli, F., 2014. Experimental investigation of counter current air–water flow in a large diameter vertical pipe with inners. J. Phys.: Conf. Ser. 547, 012024.

Besagni, G., Guédon, G.R., Inzoli, F., 2015. Annular gap bubble column: experimental investigation and CFD modeling. J. Fluids Eng.

Besagni, G., Inzoli, F., 2015. Influence of electrolyte concentration on holdup, flow regime transition and local flow properties in a large scale bubble column. J. Phys.: Conf. Ser. 655.

Besagni, G., Inzoli, F., 2016a. Influence of internals on counter-current bubble column hydrodynamics: holdup, flow regime transition and local flow properties. Chem. Eng. Sci. 145, 162–180. http://dx.doi.org/10.1016/j.ces.2016.02.019, ⟨http://www.sciencedirect.com/science/article/pii/S0009250916300641⟩.

Besagni, G., Inzoli, F., 2016b. Bubble size distributions and shapes in annular gap bubble column. Exp. Therm. Fluid Sci. 4, 27–48.

Bin, A.K., Duczmal, B., Machniewski, P., 2001. Hydrodynamics and ozone mass transfer in a tall bubble column. Chem. Eng. Sci. 56, 6233–6240.

Boyer, C., Duquenne, A.-M., Wild, G., 2002. Measuring techniques in gas–liquid and gas–liquid–solid reactors. Chem. Eng. Sci. 57, 3185–3215.

Brooks, C.S., Paranjape, S.S., Ozar, B., Hibiki, T., Ishii, M., 2012. Two-group drift-flux model for closure of the modified two-fluid model. Int. J. Heat Fluid Flow. 37, 196–208.

Busciglio, A., Grisafi, F., Scargiali, F., Brucato, A., 2010. On the measurement of local gas hold-up and interfacial area in gas–liquid contactors via light sheet and image analysis. Chem. Eng. Sci. 65, 3699–3708.

Camarasa, E., Vial, C., Poncin, S., Wild, G., Midoux, N., Bouillard, J., 1999. Influence of coalescence behaviour of the liquid and of gas sparging on hydrodynamics and bubble characteristics in a bubble column. Chem. Eng. Process.: Process. Intensif. 38, 329–344.

Cao, C., Zhao, L., Xu, D., Geng, Q., Guo, Q., 2009. Investigation into bubble size distribution and transient evolution in the Sparger region of gas – liquid external loop airlift reactors. Ind. Eng. Chem. Res. 48, 5824–5832.

Cartellier, A., Barrau, E., 1998. Monofiber optical probes for gas detection and gas velocity measurements: conical probes. Int. J. Multiph. Flow. 24, 1265–1294.

Chabot, J., Farag, H., de Lasa, H., 1998. Fluid dynamics of bubble columns at elevated temperature modelling and investigation with refractive fiber optic sensors. Chem. Eng. J. 70, 105–113.

Chang, K.-A., Lim, H.-J., Su, C.B., 2003. Fiber optic reflectometer for velocity and fraction ratio measurements in multiphase flows. Rev. Sci. Instrum. 74, 3559–3565.

Chaumat, H., Billet-Duquenne, A.M., Augier, F., Mathieu, C., Delmas, H., 2005a. Application of the double optic probe technique to distorted tumbling bubbles in aqueous or organic liquid. Chem. Eng. Sci. 60, 6134–6145.

Chaumat, H., Billet-Duquenne, A.M., Augier, F., Mathieu, C., Delmas, H., 2005b. Mass transfer in bubble column for industrial conditions—effects of organic medium, gas and liquid flow rates and column design. Chem. Eng. Sci. 60, 5930–5936.

Chaumat, H., Billet-Duquenne, A.M., Augier, F., Mathieu, C., Delmas, H., 2007. On the reliability of an optical fibre probe in bubble column under industrial relevant operating conditions. Exp. Therm. Fluid Sci. 31, 495–504.

Clift, R., Grace, J.R., Weber, M.E., 1978. Bubbles, Drops, and Particles. New York.

Dargar, P., Macchi, A., 2006. Effect of surface-active agents on the phase holdups of three-phase fluidized beds. Chem. Eng. Process.: Process. Intensif. 45, 764–772.

de Bruijn, T.J.W., Chase, J.D., Dawson, W.H., 1988. Gas holdup in a two-phase vertical tubular reactor at high pressure. Can. J. Chem. Eng. 66, 330–333.
Deckwer, W.-D., Louisi, Y., Zaidi, A., Ralek, M., 1980. Hydrodynamic properties of the Fischer–Tropsch slurry process. Ind. Eng. Chem. Process. Des. Dev. 19, 699–708.
Deckwer, W.D., 1992. Bubble Column Reactors. Wiley, Chichester.
Deshpande, N.S., Dinkar, M., Joshi, J.B., 1995. Disengagement of the gas phase in bubble columns. Int. J. Multiph. Flow. 21, 1191–1201.
Fair, J.R., Lambright, A.J., Andersen, J.W., 1962. Heat transfer and gas holdup in a sparged contactor. Ind. Eng. Chem. Process. Des. Dev. 1, 33–36.
Geary, N.W., Rice, R.G., 1991. Bubble size prediction for rigid and flexible spargers. AIChE J. 37, 161–168.
Godbole, S.P., Schumpe, A., Shah, Y.T., Carr, N.L., 1984. Hydrodynamics and mass transfer in non-Newtonian solutions in a bubble column. AIChE J. 30, 213–220.
Gopal, J.S., Sharma, M.M., 1983. Mass transfer characteristics of low H/D bubble columns. Can. J. Chem. Eng. 61, 517–526.
Gourich, B., Vial, C., Essadki, A.H., Allam, F., Belhaj Soulami, M., Ziyad, M., 2006. Identification of flow regimes and transition points in a bubble column through analysis of differential pressure signal—influence of the coalescence behavior of the liquid phase. Chem. Eng. Process.: Process. Intensif. 45, 214–223.
Hanselmann, W., Windhab, E., 1998. Flow characteristics and modelling of foam generation in a continuous rotor/stator mixer. J. Food Eng. 38, 393–405.
Hernandez-Aguilar, J.R., Coleman, R.G., Gomez, C.O., Finch, J.A., 2004. A comparison between capillary and imaging techniques for sizing bubbles in flotation systems. Miner. Eng. 17, 53–61.
Hikita, H., Kikukawa, H., 1974. Liquid-phase mixing in bubble columns: effect of liquid properties. Chem. Eng. J. 8, 191–197.
Hills, J.H., 1976. The operation of a bubble column at high throughputs: I. Gas holdup measurements. Chem. Eng. J. 12, 89–99.
Honkanen, M., Saarenrinne, P., Stoor, T., Niinimäki, J., 2005. Recognition of highly overlapping ellipse-like bubble images. Meas. Sci. Technol. 16, 1760.
Hughmark, G.A., 1967. Holdup and mass transfer in bubble columns. Ind. Eng. Chem. Process. Des. Dev. 6, 218–220.
Hur, Y.G., Yang, J.H., Jung, H., Park, S.B., 2013. Origin of regime transition to turbulent flow in bubble column: orifice- and column-induced transitions. Int. J. Multiph. Flow. 50, 89–97.
Jin, H., Yang, S., He, G., Wang, M., Williams, R.A., 2010. The effect of gas–liquid counter-current operation on gas hold-up in bubble columns using electrical resistance tomography. J. Chem. Technol. Biotechnol. 85, 1278–1283.
Jin, H., Yang, S., Wang, M., Williams, R.A., 2007. Measurement of gas holdup profiles in a gas liquid cocurrent bubble column using electrical resistance tomography. Flow Meas. Instrum. 18, 191–196.
Joshi, J.B., Veera, U.P., Parasad, C.V., Phanikkumar, D.V., Deshphande, N.S., Thakre, S. S., Thorat, B.N., 1998. Gas holdup structure in bubble column reactors. PINSA 64A, 441–567.
Kantarci, N., Borak, F., Ulgen, K.O., 2005. Bubble column reactors. Process. Biochem. 40, 2263–2283.
Karn, A., Ellis, C., Arndt, R., Hong, J., 2015. An integrative image measurement technique for dense bubbly flows with a wide size distribution. Chem. Eng. Sci. 122, 240–249.
Kataoka, I., Ishii, M., 1987. Drift flux model for large diameter pipe and new correlation for pool void fraction. Int. J. Heat Mass. Transf. 30, 1927–1939.
Kawase, Y., Moo-Young, M., 1987a. Influence of antifoam agents on gas hold-up and mass transfer in bubble columns with non-Newtonian fluids. Appl. Microbiol. Biotechnol. 27, 159–167.
Kawase, Y., Moo-Young, M., 1987b. Theoretical prediction of gas hold-up in bubble columns with Newtonian and non-Newtonian fluids. Ind. Eng. Chem. Res. 26, 933–937.
Kemoun, A., Cheng Ong, B., Gupta, P., Al-Dahhan, M.H., Dudukovic, M.P., 2001. Gas holdup in bubble columns at elevated pressure via computed tomography. Int. J. Multiph. Flow 27, 929–946.
Kiambi, S.L., Duquenne, A.-M., Dupont, J.B., Colin, C., Risso, F., Delmas, H., 2003. Measurements of bubble characteristics: comparison between double optical probe and imaging. Can. J. Chem. Eng. 81, 764–770.
Krishna, R., Urseanu, M.I., Dreher, A.J., 2000. Gas hold-up in bubble columns: influence of alcohol addition versus operation at elevated pressures. Chem. Eng. Process.: Process. Intensif. 39, 371–378.
Krishna, R., Wilkinson, P.M., Van Dierendonck, L.L., 1991. A model for gas holdup in bubble columns incorporating the influence of gas density on flow regime transitions. Chem. Eng. Sci. 46, 2491–2496.
Kumar, S., Kumar, R.A., Munshi, P., Khanna, A., 2012. Gas hold-up in three phase co-current bubble columns. Procedia Eng. 42, 782–794.
Lage, P.L.C., Espósito, R.O., 1999. Experimental determination of bubble size distributions in bubble columns: prediction of mean bubble diameter and gas hold up. Powder Technol. 101, 142–150.
Lau, R., Peng, W., Velazquez-Vargas, L.G., Yang, G.Q., Fan, L.S., 2004. Gas–liquid mass transfer in high-pressure bubble columns. Ind. Eng. Chem. Res. 43, 1302–1311.
Lau, Y.M., Deen, N.G., Kuipers, J.A.M., 2013a. Development of an image measurement technique for size distribution in dense bubbly flows. Chem. Eng. Sci. 94, 20–29.
Lau, Y.M., Sujatha, K.T., Gaeini, M., Deen, N.G., Kuipers, J.A.M., 2013b. Experimental study of the bubble size distribution in a pseudo-2D bubble column. Chem. Eng. Sci. 98, 203–211.
Lecuona, A., Sosa, P.A., Rodríguez, P.A., Zequeira, R.I., 2000. Volumetric characterization of dispersed two-phase flows by digital image analysis. Meas. Sci. Technol. 11, 1152.
Leonard, C., Ferrasse, J.H., Boutin, O., Lefevre, S., Viand, A., 2015. Bubble column reactors for high pressures and high temperatures operation. Chem. Eng. Res. Des. 100, 391–421.
Letzel, H.M., Schouten, J.C., Krishna, R., van den Bleek, C.M., 1999. Gas holdup and mass transfer in bubble column reactors operated at elevated pressure. Chem. Eng. Sci. 54, 2237–2246.
Letzel, H.M., Schouten, J.C., van den Bleek, C.M., Krishna, R., 1997. Influence of elevated pressure on the stability of bubbly flows. Chem. Eng. Sci. 52, 3733–3739.
Lima Neto, I., Zhu, D., Rajaratnam, N., 2008. Air injection in water with different nozzles. J. Environ. Eng. 134, 283–294.
Lu, J., Biswas, S., Tryggvason, G., 2006. A DNS study of laminar bubbly flows in a vertical channel. Int. J. Multiph. Flow 32, 643–660.
Lu, J., Tryggvason, G., 2007. Effect of bubble size in turbulent bubbly downflow in a vertical channel. Chem. Eng. Sci. 62, 3008–3018.
Lu, J., Tryggvason, G., 2013. Dynamics of nearly spherical bubbles in a turbulent channel upflow. J. Fluid Mech. 732, 166–189.
Lucas, D., Krepper, E., Prasser, H.M., 2003. Evolution of flow patterns, gas fraction profiles and bubble size distributions in gas–liquid flows in vertical tubes. Trans. Inst. Fluid-Flow Mach. 112, 37–46.
Lucas, D., Prasser, H.M., Manera, A., 2005. Influence of the lift force on the stability of a bubble column. Chem. Eng. Sci. 60, 3609–3619.
Lucas, D., Rzehak, R., Krepper, E., Ziegenhein, T., Liao, Y., Kriebitzsch, S., Apanasevich, P., 2015. A strategy for the qualification of multi-fluid approacheds for nuclear reactor safety. Nucl. Eng. Des. ⟨http://dx.doi.org/10.1016/j.nucengdes.2015.07.007⟩
Magaud, F., Souhar, M., Wild, G., Boisson, N., 2001. Experimental study of bubble column hydrodynamics. Chem. Eng. Sci. 56, 4597–4607.
Mashelkar, R., 1970. Bubble columns. Br. Chem. Eng. 15, 1297 1297.
Miyahara, T., Hayashino, T., 1995. Size of bubbles generated from perforated plates in non-Newtonian liquids. J. Chem. Eng. Jpn. 28, 596–600.
Moujaes, S.F., 1990. Testing of a spherical dual-tipped optical fiber probe for local measurements of void fraction and gas velocity in two-phase flows. Can. J. Chem. Eng. 68, 504–510.
Mudde, R.F., Harteveld, W.K., van den Akker, H.E.A., 2009. Uniform flow in bubble columns. Ind. Eng. Chem. Res. 48, 148–158.
Nedeltchev, S., 2015. New methods for flow regime identification in bubble columns and fluidized beds. Chem. Eng. Sci. 137, 436–446.
Nedeltchev, S., Schubert, M., 2015. Statistical validation of the mixing length concept in bubble columns operated in the transition flow regime. J. Chem. Eng. Jpn. 48, 107–111.
Nedeltchev, S., Shaikh, A., 2013. A new method for identification of the main transition velocities in multiphase reactors based on information entropy theory. Chem. Eng. Sci. 100, 2–14.
Otake, T., Tone, S., Shinohara, K., 1981. Gas holdup in the bubble column with cocurrent and countercurrent gas–liquid flow. J. Chem. Eng. Jpn., 338–340.
Parthasarathy, R., Ahmed, N., 1994. Bubble size distribution in a gas sparged vessel agitated by a rushton turbine. Ind. Eng. Chem. Res. 33, 703–711.
Passos, A.D., Voulgaropoulos, V.P., Paras, S.V., Mouza, A.A., 2015. The effect of surfactant addition on the performance of a bubble column containing a non-Newtonian liquid. Chem. Eng. Res. Des. 95, 93–104.
Pjontek, D., Parisien, V., Macchi, A., 2014. Bubble characteristics measured using a monofibre optical probe in a bubble column and freeboard region under high gas holdup conditions. Chem. Eng. Sci. 111, 153–169.
Polli, M., Stanislao, M.D., Bagatin, R., Bakr, E.A., Masi, M., 2002. Bubble size distribution in the sparger region of bubble columns. Chem. Eng. Sci. 57, 197–205.
Rakoczy, R., Masiuk, S., 2009. Experimental study of bubble size distribution in a liquid column exposed to a rotating magnetic field. Chem. Eng. Process.: Process. Intensif. 48, 1229–1240.
Reilly, I., Scott, D., Debruijn, T., MacIntyre, D., 1994. The role of gas phase momentum in determining gas holdup and hydrodynamic flow regimes in bubble column operations. Can. J. Chem. Eng. 72, 3–12.
Reilly, I.G., Scott, D.S., De Bruijn, T., Jain, A., Piskorz, J., 1986. A correlation for gas holdup in turbulent coalescing bubble columns. Can. J. Chem. Eng. 64, 705–717.
Ribeiro Jr, C.P., Mewes, D., 2007. The influence of electrolytes on gas hold-up and regime transition in bubble columns. Chem. Eng. Sci. 62, 4501–4509.
Richardson, J.F., Zaki, W.N., 1997. Sedimentation and fluidisation: part I. Chem. Eng. Res. Des. 75 (Supplement), S82–S100.
Rodrigues, R.T., Rubio, J., 2003. New basis for measuring the size distribution of bubbles. Miner. Eng. 16, 757–765.
Rodríguez-Rodríguez, J., Martínez-Bazán, C., Montañes, J.L., 2003. A novel particle tracking and break-up detection algorithm: application to the turbulent break-up of bubbles. Meas. Sci. Technol. 14, 1328.
Rollbusch, P., Becker, M., Ludwig, M., Bieberle, A., Grünewald, M., Hampel, U., Franke, R., 2015a. Experimental investigation of the influence of column scale, gas density and liquid properties on gas holdup in bubble columns. Int. J. Multiph. Flow 75, 88–106.
Rollbusch, P., Bothe, M., Becker, M., Ludwig, M., Grünewald, M., Schlüter, M., Franke, R., 2015b. Bubble columns operated under industrially relevant conditions – current understanding of design parameters. Chem. Eng. Sci. 126, 660–678.
Ruzicka, M.C., Drahovs, J., Fialova, M., Thomas, N.H., 2001. Effect of bubble column dimensions on flow regime transition. Chem. Eng. Sci. 56, 6117–6124.
Sada, E., Katoh, S., Yoshii, H., Yamanishi, T., Nakanishi, A., 1984. Performance of the gas bubble column in molten salt systems. Ind. Eng. Chem. Process. Des. Dev. 23, 151–154.

Sangnimnuan, A., Prasad, G.N., Agnew, J.B., 1984. Gas hold-up and backmixing in a bubble-column reactor under coal-hydroliquefaction conditions. Chem. Eng. Commun. 25, 193–212.

Santarelli, C., Fröhlich, J., 2016. Direct Numerical Simulations of spherical bubbles in vertical turbulent channel flow. Influence of bubble size and bidispersity. Int. J. Multiph. Flow 81, 27–45 < http://www.sciencedirect.com/science/article/pii/S0301932216000045 > .

Schäfer, R., Merten, C., Eigenberger, G., 2002. Bubble size distributions in a bubble column reactor under industrial conditions. Exp. Therm. Fluid Sci. 26, 595–604.

Schumpe, A., Grund, G., 1986. The gas disengagement technique for studying gas holdup structure in bubble columns. Can. J. Chem. Eng. 64, 891–896.

Shah, M., Kiss, A.A., Zondervan, E., Van Der Schaaf, J., De Haan, A.B., 2012. Gas holdup, axial dispersion, and mass transfer studies in bubble columns. Ind. Eng. Chem. Res. 51, 14268–14278.

Shah, Y.T., Kelkar, B.G., Godbole, S.P., Deckwer, W.D., 1982. Design parameters estimations for bubble column reactors. AIChE J. 28, 353–379.

Shawaqfeh, A.T., 2003. Gas holdup and liquid axial dispersion under slug flow conditions in gas–liquid bubble column. Chem. Eng. Process.: Process. Intensif. 42, 767–775.

Shawkat, M.E., Ching, C.Y., 2011. Liquid turbulence kinetic energy budget of co-current bubbly flow in a large diameter vertical pipe. J. Fluids Eng. 133, 091303 091303.

Shiea, M., Mostoufi, N., Sotudeh-Gharebagh, R., 2013. Comprehensive study of regime transitions throughout a bubble column using resistivity probe. Chem. Eng. Sci. 100, 15–22.

Simonnet, M., Gentric, C., Olmos, E., Midoux, N., 2007. Experimental determination of the drag coefficient in a swarm of bubbles. Chem. Eng. Sci. 62, 858–866.

Sundaresan, A., Varma, Y., 1990. Dispersed phase holdup and bubble size distributions in gas–liquid cocurrent upflow and countercurrent flow in reciprocating plate column. Can. J. Chem. Eng. 68, 560–568.

Thorat, B.N., Shevade, A.V., Bhilegaonkar, K.N., Aglawe, R.H., Parasu Veera, U., Thakre, S.S., Pandit, A.B., Sawant, S.B., Joshi, J.B., 1998. Effect of sparger design and height to diameter ratio on fractional gas hold-up in bubble columns. Chem. Eng. Res. Des. 76, 823–834.

Tomiyama, A., Tamai, H., Zun, I., Hosokawa, S., 2002. Transverse migration of single bubbles in simple shear flows. Chem. Eng. Sci. 57, 1849–1858.

Urseanu, M.I., 2000. Scaling up bubble column reactors.

Vejražka, J., Večeř, M., Orvalho, S., Sechet, P., Ruzicka, M.C., Cartellier, A., 2010. Measurement accuracy of a mono-fiber optical probe in a bubbly flow. Int. J. Multiph. Flow 36, 533–548.

Voigt, J., Schügerl, K., 1979. Absorption of oxygen in countercurrent multistage bubble columns—I aqueous solutions with low viscosity. Chem. Eng. Sci. 34, 1221–1229.

Wallis, G.B., 1969. One-dimensional two-phase flow. New York.

Wilkinson, P.M., Spek, A.P., van Dierendonck, L.L., 1992. Design parameters estimation for scale-up of high-pressure bubble columns. AIChE J. 38, 544–554.

Wongsuchoto, P., Charinpanitkul, T., Pavasant, P., 2003. Bubble size distribution and gas–liquid mass transfer in airlift contactors. Chem. Eng. J. 92, 81–90.

Xu, C., Shepard, T., 2014. Digital image processing algorithm for determination and measurement of in-focus spherical bubbles. In: Proceedings of ASME 2014 4th Joint US-European Fluids Engineering Division Summer Meeting collocated with the ASME 2014 12th International Conference on Nanochannels, Microchannels, and Minichannels. American Society of Mechanical Engineers. pp. V01BT22A002–V001BT022A002.

Yamaguchi, K., Yamazaki, Y., 1982a. Characteristics of counter current gas–liquid two-phase flow in vertical tubes. J. Nucl. Sci. Technol. 19, 985–996.

Yamaguchi, K., Yamazaki, Y., 1982b. Characteristics of countercurrent gas–liquid two-phase flow in vertical tubes. J. Nucl. Sci. Technol. 19, 985–996.

Yang, G.Q., Fan, L.S., 2003. Axial liquid mixing in high-pressure bubble columns. AIChE J. 49, 1995–2008.

Ying, D.H., Moujaes, S., Sivasubramanian, R., Givens, E., 1981. Gas/slurry Flow in Coal-Liquefaction Processes (fluid dynamics in 3-phase-flow column). Air Products and Chemicals, Inc.,, Allentown, PA (USA).

Yoshida, F., Akita, K., 1965. Performance of gas bubble columns: volumetric liquid-phase mass transfer coefficient and gas holdup. AIChE J. 11, 9–13.

Zahradnik, J., Fialova, M., Rruvzivc, k, M., Drahovs, J., Kavstanek, F., Thomas, N.H., 1997. Duality of the gas–liquid flow regimes in bubble column reactors. Chem. Eng. Sci. 52, 3811–3826.

Zaruba, A., Krepper, E., Prasser, H.M., Schleicher, E., 2005. Measurement of bubble velocity profiles and turbulent diffusion coefficients of the gaseous phase in rectangular bubble column using image processing. Exp. Therm. Fluid Sci. 29, 851–860.

Zhang, W., Zhu, D.Z., 2013. Bubble characteristics of air–water bubbly jets in crossflow. Int. J. Multiph. Flow 55, 156–171.

Zuber, N., Findlay, J.A., 1965. Average volumetric concentration in two-phase flow systems. J. Heat Transf. 87, 453–468.